

**Numerical simulation of thermal stratification in Lake Qiandaohu using an improved WRF-Lake model**

Wang, Xiwen; Wang, Weijia; He, Yuan; Zhang, Shulei; Huang, Wei; Woolway, R. Iestyn; Shi, Kun; Yang, Xiaofan

Journal of Hydrology

DOI:

[10.1016/j.jhydrol.2023.129184](https://doi.org/10.1016/j.jhydrol.2023.129184)

Published: 01/03/2023

Peer reviewed version

[Cyswllt i'r cyhoeddiad / Link to publication](#)

Dyfyniad o'r fersiwn a gyhoeddwyd / Citation for published version (APA):

Wang, X., Wang, W., He, Y., Zhang, S., Huang, W., Woolway, R. I., Shi, K., & Yang, X. (2023). Numerical simulation of thermal stratification in Lake Qiandaohu using an improved WRF-Lake model. *Journal of Hydrology*, 618, Article 129184. <https://doi.org/10.1016/j.jhydrol.2023.129184>

Hawliau Cyffredinol / General rights

Copyright and moral rights for the publications made accessible in the public portal are retained by the authors and/or other copyright owners and it is a condition of accessing publications that users recognise and abide by the legal requirements associated with these rights.

- Users may download and print one copy of any publication from the public portal for the purpose of private study or research.
- You may not further distribute the material or use it for any profit-making activity or commercial gain
- You may freely distribute the URL identifying the publication in the public portal ?

Take down policy

If you believe that this document breaches copyright please contact us providing details, and we will remove access to the work immediately and investigate your claim.

1 **Numerical simulation of thermal stratification in Lake Qiandaohu using an**
2 **improved WRF-Lake model**

3

4 Xiwen Wang^{a,b}, Weijia Wang^{b,c}, Yuan He^d, Shulei Zhang^e, Wei Huang^a, R. Iestyn
5 Woolway^f, Kun Shi^{b,c*}, Xiaofan Yang^{d*}

6 ^aKey Laboratory of Western China's Environmental Systems (Ministry of Education),
7 College of Earth and Environmental Sciences, Lanzhou University, Lanzhou, 730000,
8 China

9 ^b Taihu Laboratory for Lake Ecosystem Research, State Key Laboratory of Lake
10 Science and Environment, Nanjing Institute of Geography and Limnology, Chinese
11 Academy of Sciences, Nanjing 210008, China

12 ^c University of Chinese Academy of Sciences, Beijing 100049, China

13 ^d State Key Laboratory of Earth Surface Processes and Resource Ecology, Faculty of
14 Geographical Science, Beijing Normal University, Beijing 100875, China

15 ^e School of Atmospheric Sciences, Sun Yat-sen University, Guangzhou, China

16 ^f School of Ocean Sciences, Bangor University, Menai Bridge, Anglesey, Wales

17

18 Corresponding author:

19 Kun Shi: kshi@niglas.ac.cn

20 Xiaofan Yang: xfyang@bnu.edu.cn

21

22 **Abstract**

23 Lake thermal stratification is important for regulating lake environments and
24 ecosystems and is sensitive to climate change and human activity. However,
25 numerical simulation of coupled hydrodynamics and heat transfer processes in deep
26 lakes using one-dimensional lake models remains challenging because of the
27 insufficient representation of key parameters. In this study, Lake Qiandaohu, a deep
28 and warm monomictic reservoir, was used as an example to investigate thermal
29 stratification via an improved parameterization scheme of the Weather Research and
30 Forecast (WRF)-Lake. A comparison with in situ observations demonstrated that the
31 default WRF-Lake model was able to simulate well the seasonal variation of the lake
32 thermal structure. However, the simulations exhibited cold biases in lake surface
33 water temperature (LSWT) throughout the year while generating weaker stratification
34 in summer, thereby leading to an earlier cooling period in autumn. With an improved
35 parameterization (i.e., via determination of initial lake water temperature profiles,
36 light extinction coefficients, eddy diffusion coefficients and surface roughness
37 lengths), the modified WRF-Lake model was able to better simulate LSWT and
38 thermal stratification. Critically, employing realistic initial conditions for lake water
39 temperature is essential for producing realistic hypolimnetic water temperatures. The
40 use of time-dependent light extinction coefficients resulted in a deep thermocline and
41 warm LSWT. Enlarging eddy diffusivity led to stronger mixing in summer and further
42 influenced autumn cooling. The parameterized surface roughness lengths mitigated

43 the excessive turbulent heat loss at the lake surface, improved the model performance
44 in simulating LSWT, and generated a warm mixed layer. This study provides
45 guidance on model parameterization for simulating the thermal structure of deep lakes
46 and advances our understanding of the strength and revolution of lake thermal
47 stratification under seasonal changes.

48

49 **Keywords:** Thermal stratification; Lake/reservoir; Numerical simulation; WRF-Lake;
50 Parameter sensitivity

51

52

53 1. Introduction

54 Thermal stratification is an important physical process in many lakes/reservoirs
55 that modulates their response to climate change and maintains lake ecosystem
56 functions (Donis et al., 2021; Till et al., 2019). Stratification in lakes is mediated by
57 the complex non-linear interactions between the lake surface and the atmosphere. It is
58 influenced by atmospheric forcing and lake-specific properties, such as water
59 transparency and geomorphological (depth, surface area) factors (Kraemer et al., 2015;
60 Richardson et al., 2017). Although recent studies have reported a mixing regime shift
61 in large lakes (Anderson et al., 2021), a fundamental and predictive understanding of
62 lake stratification is still obscured due to the scarcity of in situ observations.
63 Numerical simulations provide an opportunity to compensate for the space and time
64 limitations of observations (Piccolroaz et al., 2020) and diagnose the effects of
65 potential impact factors (Woolway et al., 2020; Woolway et al., 2019). Growing
66 computational power further allows the coupling of lake and climate models to
67 simulate lake–atmosphere interactions. However, the demand for computing
68 efficiency in large-scale and long-term simulations restricts the application of
69 sophisticated three-dimensional hydrodynamic models (Zamani et al., 2021). One-
70 dimensional (1D) lake models, which simplify lake physical processes but require
71 relatively minimal calibration, have been demonstrated to be effective tools for
72 simulating thermal stratification at larger scales (Bruce et al., 2018; Stepanenko et al.,
73 2010).

74 There are two types of one-dimensional lake models based on different
75 numerical discretization methods: bulk (or integral) models and models based on the
76 finite-difference scheme (Stepanenko et al., 2010). For example, the Freshwater Lake
77 model (FLake) (Mironov, 2008), as a representative bulk lake model, has been
78 incorporated into a set of climate models with high computational efficiency
79 (Balsamo et al., 2012; Thiery et al., 2014b). Evaluations of the FLake model have
80 shown that it is suitable for reproducing LSWT and thermal structure in shallow lakes
81 but fails to simulate the development of thermal stratification in deep lakes as it does
82 not directly solve the physical processes (Huang et al., 2019; Thiery et al., 2014a).
83 The models based on the finite-difference scheme include eddy diffusion models and
84 turbulent-kinetic (k - ϵ) models (Perroud et al., 2009). Eddy diffusion models use semi-
85 empirical parameterization for the representation of turbulent fluxes. The k - ϵ models
86 solve two equations including turbulent kinetic energy and its dissipation rate. Eddy
87 diffusion models are inexpensive and proven to produce more accurate epilimnion
88 temperature, whereas the k - ϵ models are more complicated but performed better for
89 simulating thermocline depth (Guo et al., 2021). Eddy diffusion models are ideal
90 candidates for coupling to climate/earth system models because of their relatively low
91 cost and better representation of mixing processes compared to FLake. For example,
92 the Hostetler lake model and its successors have been implemented in the community
93 land surface model (CLM-Lake) (Oleson et al., 2013), common land model (CoLM-
94 Lake) (Dai et al., 2018a), and the Weather Research and Forecast model (WRF-Lake)

95 (Gu et al., 2015). Previous studies have shown that the lake component of WRF-Lake
96 outperformed FLake and other lake models based on turbulent closure schemes when
97 simulating summer stratification in Lake Valkea-Kotinen, a small shallow lake in
98 southern Finland (Stepanenko et al., 2014). It has also been suggested that WRF-Lake
99 better describes the temporal variation of the total water column temperature than
100 FLake and CoLM-Lake in Lake Nam Co, a large and deep lake on the Qinghai-Tibet
101 Plateau (Huang et al., 2019). Hostetler model shows smaller biases compared to those
102 utilizing more complicated algorithms when used for global application (Guo et al.,
103 2021) and offers a marked degree of flexibility for specific lake applications
104 (Martynov et al., 2010).

105 The WRF-Lake model has been utilized to simulate physical processes in a
106 variety of lakes, from shallow to deep systems as well as those situated across warm
107 and cold climatic regions (Gu et al., 2015; Gu et al., 2016; Huang et al., 2019; Su et
108 al., 2022; Wu et al., 2020; Xiao et al., 2016; Xu et al., 2016). The performance of
109 WRF-Lake is highly sensitive to key model parameters, notably the eddy diffusivity,
110 light extinction coefficient, temperature of maximum water density for brackish water
111 simulations, and surface roughness lengths of lake surface (Huang et al., 2019). These
112 parameters are lake-specific and simplified in WRF-Lake. Such simplification may be
113 sufficient for global-scale analysis, in which the uncertainties for specific lakes of a
114 single model can either be filtered directly or compensated by ensemble simulations
115 to reveal large-scale patterns. But for regional-scale simulations, the model

116 parameters related to lake characteristics have to be carefully tuned to achieve the
117 required accuracy. Gu et al. (2015) suggested that although LSWT in relatively
118 shallow lakes (e.g., Lake Erie) can be well captured, the vertical heat transfer process
119 predicted by WRF-Lake is underestimated for deep lakes (e.g., Lake Superior) and
120 leads to large biases in LSWT. Previous parameter sensitivity analyses demonstrated
121 that the deficiency of WRF-Lake can be improved by enlarging the eddy diffusivity
122 by a factor of 10^2 – 10^5 , which has been proven to be effective in simulating the
123 thermal structure of Lake Nam Co (Huang et al., 2019; Wu et al., 2020). However,
124 another study at the Laurentian Great Lakes found that the parameterization scheme
125 presented by Gu et al. (2015) only exerted a limited influence on Lake Michigan (~
126 147.5 m at the mooring site) (Xiao et al., 2016). A recent study based on the offline
127 version of WRF-Lake in the deep Reservoir Nuozhadu utilized a more elaborate
128 calibration for eddy diffusivity, in which an enhanced term was added and enlarged
129 for deep layers (Wang et al., 2019). Therefore, it is evident that the influence and
130 uncertainty of eddy diffusivity on simulating thermal structures in deep lakes are quite
131 diverse yet unclear, which requires proper calibration in different lakes.

132 Moreover, the light extinction coefficient can substantially alter the thermal
133 structure of lakes by regulating the vertical heat transfer process (Read and Rose,
134 2013; Rose et al., 2016). For example, larger light extinction coefficients will lead to
135 more absorbed shortwave radiation, resulting in thicker mixed layers (Wang et al.,
136 2019); reducing light extinction coefficients in clearwater lakes may deepen the

137 thermocline and generate a warmer mixed layer (Wu et al., 2020). Previous studies on
138 modifying the light extinction coefficient were primarily based on empirical
139 estimations that neglected the seasonal fluctuation of lake water clarity caused by
140 phytoplankton growth (Shatwell et al., 2016).

141 Lake Qiandaohu is located in the hilly areas of Zhejiang Province in eastern
142 China. It has a complex morphology and remains thermally stratified throughout the
143 year. Lake Qiandaohu is a warm monomictic lake and experiences short-term mixing
144 in winter or spring (Zhang et al., 2014). Thermal stratification in Lake Qiandaohu
145 usually begins in March and becomes the most intense in August and lasts until
146 December, with a temperature difference between the surface and bottom ranging
147 from 5 °C to 20 °C (Liu et al., 2019; Zhang et al., 2014). Although the phenology of
148 its stratification has been well documented, the influencing mechanisms and evolution
149 of lake physical characteristics (e.g. the water clarity and mixing process) are not clear.
150 Proper parameterization in simulating the stratification in Lake Qiandaohu, as a
151 representative of deep and warm monomictic lakes, would help to understand the
152 evolution of the lake thermal structure. This study aims to: (1) improve the
153 fundamental understanding of the thermal structure of Lake Qiandaohu, (2) address
154 the influencing mechanism of key model parameters, and (3) provide references for
155 WRF-Lake application in deep lakes. To achieve these goals, six sensitivity
156 experiments were conducted in Lake Qiandaohu in 2016. This paper is organized as
157 follows: Section 2 describes the WRF-Lake model configuration and numerical

158 experiments, and simulation results are presented in Section 3 and interpreted in
159 Section 4. The major findings of this study are presented in Section 5.

160

161 **2. Numerical modeling and simulation**

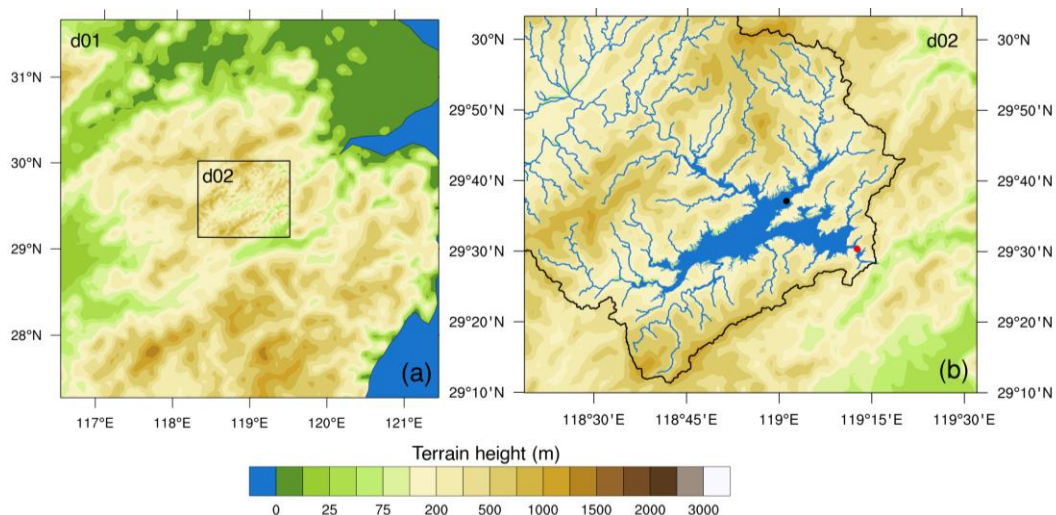
162 **2.1. Site description**

163 Lake Qiandaohu (29.37–29.83 °N, 118.57–119.25 °E) is a deep reservoir in
164 eastern China and means “thousand island archipelagoes” in Chinese; it was
165 established in 1959. It is a nationally protected drinking water source, with a basin
166 area of 10480 km² and a water volume of 178.4×10^8 m³ when the normal water
167 storage water level is 108 m (Zhang et al., 2014). It has a water surface area of 580
168 km² with a length and width of 150 km and 50 km, respectively, at its widest point
169 (Zhang et al., 2014). Lake Qiandaohu is morphologically complex and contains five
170 sub-basins, the deepest of which is 105 m, although the average depth of the lake is
171 only 30 m (Zhang et al., 2014).

172 **2.2. WRF model configurations**

173 The Weather Research and Forecasting model version 4.0 (hereafter referred to
174 as “WRF”) (<https://www2.mmm.ucar.edu/wrf/users>) is a state-of-the-art numerical
175 weather prediction model. It solves the fully compressible Euler non-hydrostatic
176 equations using the Arakawa-C staggered grid, second- or third-order Runge-Kutta
177 time integration scheme, and terrain-following vertical coordinate system (Skamarock
178 et al., 2019).

179 In this study, the WRF model was configured with two one-way nested domains
180 with horizontal resolutions of 5 km and 1 km, centered on Lake Qiandaohu (Figure 1),
181 with 33 levels in the vertical direction. The selection of horizontal spacing considers
182 both the computational efficiency and complex shape of Lake Qiandaohu. After
183 several tests, the Yonsei University (YSU) planetary boundary layer scheme (Hong et
184 al., 2006) and topographic correction method proposed by Jiménez and Dudhia (2012)
185 were chosen to reach the minimum bias of wind speed. The Betts-Miller-Janjic
186 cumulus convection scheme (Janjic, 1994) was applied to the outer 5 km resolution
187 domain only. The Noah land surface scheme (Chen and Dudhia, 2001), WSM6
188 microphysics scheme (Lim and Hong, 2006), revised MM5 surface layer scheme
189 (Jiménez et al., 2012) and UCM urban surface scheme (Chen et al., 2011) are also
190 affiliated. To improve the atmospheric simulation, the temperature, humidity, and
191 horizontal wind fields above the planetary boundary layer of the outer domain were
192 nudged to the ERA5 reanalysis by employing analysis nudging (Stauffer and Seaman,
193 1994).



194

195 Figure 1. (a) Simulation domain with terrain height (m). The inner (1 km) grids are
196 outlined in black. (b) Inner WRF grid and terrain height (m). The black dot and red
197 dot in (b) denote the location of the Chun'an weather station and Daba buoy,
198 respectively.

199 **2.3. Simulating lake processes using WRF-Lake**

200 **2.3.1. Lake scheme of WRF-Lake**

201 The lake scheme of WRF-Lake was derived from CLM 3.5, which was
202 embedded into the WRF model (Gu et al., 2015). WRF-Lake is a 1D advection-
203 diffusion lake model that discretizes the water column vertically into 0–5 snow layers,
204 10 water/ice layers, and 10 soil layers. The layer thickness of the first water/ice layer
205 is always set to 10 cm and the other layer thickness is adjusted with fixed proportion.
206 Taking the location of the Daba buoy as an example (~ 93 m), the layer depths (m) for
207 the ten water/ice layers are listed as follows: 0.05, 4.75, 14.05, 23.35, 32.65, 41.95,
208 51.25, 60.55, 69.85, 79.15. The layer thickness is 0.1 m for the first layer and 9.3 m
209 for the rest. We also performed numerical experiments using a 25-layer discretization
210 scheme (as a grid-independence check, see Supporting Information 2). We found that
211 although the 25-layer scheme generated smoother vertical water temperature profiles,
212 the overall pattern of lake thermal structure was similar to that of the ten-layer one.
213 Variations in lake water level and area are not considered in WRF-Lake.

214 The exchange of heat, moisture and momentum between the lake and overlying
215 atmosphere is governed by the energy budget equation (Oleson et al., 2004) as:

$$216 \quad \beta \vec{S}_g - \vec{L}_g - SH_{\uparrow} - LH_{\uparrow} - G_{\downarrow} = 0 \quad (1)$$

$$217 \quad \vec{S}_g = (1 - \alpha)SW_{\downarrow} \quad (2)$$

$$218 \quad \vec{L}_g = \varepsilon\sigma T_g^4 - LW_{\downarrow} \quad (3)$$

219 where $\beta = 0.4$ is the fraction of the solar radiation absorbed at the lake surface; \vec{S}_g is
 220 the net shortwave radiation (W m^{-2}); \vec{L}_g is the net emitted longwave radiation (W m^{-2});
 221 SH_{\uparrow} is the turbulent flux of sensible heat (W m^{-2}); LH_{\uparrow} is the turbulent flux of latent
 222 heat (W m^{-2}); G_{\downarrow} is the net heat flux into the ground (W m^{-2}); α is the lake surface
 223 albedo; SW_{\downarrow} is the downward shortwave radiation (W m^{-2}); $\varepsilon = 0.97$ is the lake
 224 surface emissivity; $\sigma = 5.67 \times 10^{-8} \text{ W m}^{-2} \text{ K}^{-4}$ (Stefan-Boltzmann constant); T_g is
 225 the lake surface temperature (K); and LW_{\downarrow} is the downward atmospheric longwave
 226 radiation (W m^{-2}). Eqn. (1) is solved numerically by the Newton-Raphson iteration
 227 method to derive T_g and turbulent fluxes.

228 Subsurface energy transport is governed by the 1D heat diffusion equation
 229 (Hostetler and Bartlein, 1990; Oleson et al., 2004) and is expressed as follows:

$$230 \quad \frac{\partial T}{\partial t} = \frac{\partial}{\partial z} \left[(k_m + k_e) \frac{\partial T}{\partial z} \right] - \frac{1}{c_w} \frac{d\phi}{dz} \quad (4)$$

231 where T is the lake temperature (K), t is time (s), $k_m = 1.43 \times 10^{-7} \text{ m}^2 \text{ s}^{-1}$ is the
 232 molecular diffusion coefficient, k_e is the eddy diffusion coefficient ($\text{m}^2 \text{ s}^{-1}$), c_w is the
 233 volumetric heat capacity ($\text{J m}^{-3} \text{ K}^{-1}$), and $\phi = (1 - \beta)\vec{S}_g \exp^{-\eta(\max(z-z_s, 0))}$ is the solar
 234 radiation (W m^{-2}) penetrating to depth z (m); where $\eta = 1.1925d^{-0.424}$ is the light
 235 extinction coefficient (m^{-1}) as a function of lake depth d (m), and $z_s = 0.6$ m is the
 236 thickness of the surface layer.

237 In WRF-Lake, the mixing process is described using an advection-diffusion
 238 model (Eqn. 4), whereby the eddy diffusion coefficient k_e for layer i was calculated
 239 from the wind speed as described by Oleson et al. (2004):

$$240 \quad k_{e,i} = \begin{cases} \frac{k w^* z_i}{P_0(1 + 37R_i^2)} \exp(-k^* z_i) & , T_g > T_f \\ 0 & , T_g \leq T_f \end{cases} \quad (5)$$

241 where $k = 0.4$ is the Von Karman constant; $w^* = 0.0012u_2$ is the surface friction
 242 velocity (m s^{-1}), where $u_2 = \min(\frac{u_*}{k} \ln(\frac{z}{z_{om}}, 0.1)$ is the 2-m wind speed (m s^{-1})
 243 calculated; z_i is the node depth (m); $P_0 = 1$ is the neutral value of the turbulent
 244 Prandtl number; R_i is the Richardson number given below; and k^* varies with latitude
 245 φ as $k^* = 6.6u_2^{-1.84} \sqrt{|\sin \varphi|}$.

246 The Richardson number R_i is defined as:

$$247 \quad R_i = \frac{-1 + \sqrt{1 + \frac{40N^2 k^2 z_i^2}{w^{*2} \exp(-2k^* z_i)}}}{20} \quad (6)$$

248 where N^2 is the buoyancy frequency (s^{-2})

$$249 \quad N^2 = \frac{g}{\rho_i} \frac{\partial \rho}{\partial z} \quad (7)$$

250 where g is the acceleration due to gravity and ρ_i is the density of water (kg m^{-3}).

251 2.3.2. Eddy diffusivity calculation from in situ measurements

252 The flux gradient method can be used to determine the eddy diffusivity k_e from
 253 in situ temperature measurements by integrating Eqn. (4) from depth z to the lake
 254 bottom at depth d while assuming that the turbulent heat flux and net radiation at the
 255 lake bottom are equal to zero (Powell and Jassby, 1974). Thus, k_e can be derived
 256 explicitly from the following expression:

257
$$k_e(z) = \left(\int_z^d \frac{\partial T}{\partial t} dz - \frac{1}{c_w} \phi(z) \right) / \frac{-\partial T}{\partial z} - k_m \quad (8)$$

258 where ϕ is calculated consistent with the procedure used in WRF-Lake.

259 Eqn. (8) is valid only below the mixed layer, where the heat transfer caused by
 260 convective mixing and horizontal advection can be neglected (Powell and Jassby,
 261 1974). The 30-day averages of the lake water temperature and ϕ were used to
 262 estimate k_e at the center of this time interval. The 30-day averaging was used to
 263 smooth the profiles of k_e to better illustrate its variation with depth and time. Central-
 264 difference and forward-difference approximations were used for the spatial and time
 265 derivatives with $\Delta z = 0.5$ m and $\Delta t = 30$ days, respectively. The trapezoidal rule was
 266 applied for approximating the integral with a 0.5 m subinterval. Negative values due
 267 to cooling of the water column or unstable water layers are excluded from the results.

268 **2.4. Improvements to the WRF-Lake model**

269 **2.4.1. Initial lake water temperature profile**

270 The default initial lake water temperature in the WRF-Lake was derived from the
 271 ground temperature T_g as follows:

272
$$T_i = \begin{cases} T_g & , i = 1 \\ T_g + \frac{z_i(277 - T_g)}{50} & , z_i \leq 50 \\ 277 & , z_i > 50 \end{cases} \quad (9)$$

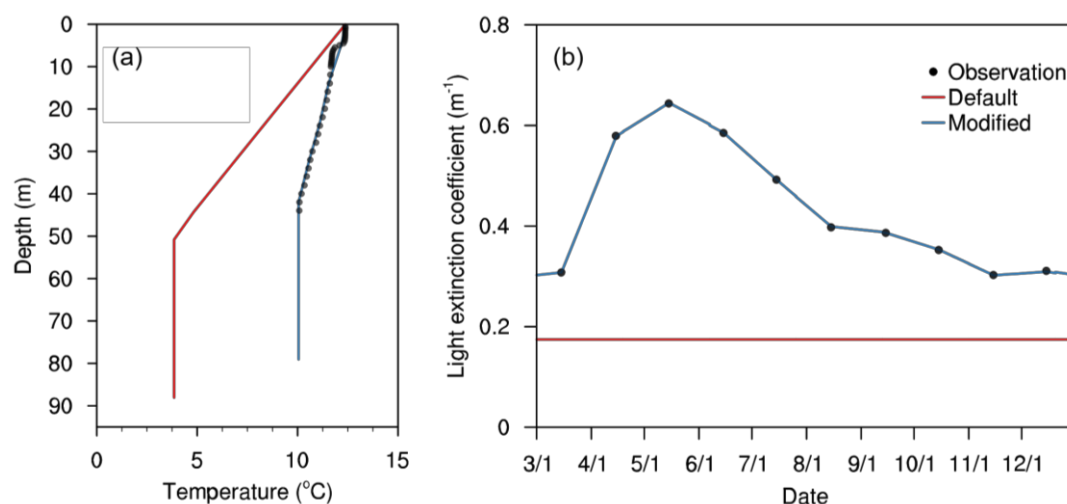
273 Where the layer $i = 1$ denotes the top layer. We note that Eqn. (8) was derived from
 274 the observed lake temperature profile of Lake Superior. In the simulation results using
 275 the default lake scheme, the initialization procedure generated a large surface-bottom
 276 water temperature difference of 8.53 °C, which is substantially higher than the

277 observed data (2.29 °C). Overestimation of the initial lake water temperature gradients
278 resulted in unrealistic cold biases for the lake bottom water temperature throughout
279 the year. For lakes that regularly experience complete turnover, it can be assumed that
280 the lake is fully mixed with a homogeneous temperature profile as the initial condition
281 (Wu et al., 2020). However, Lake Qiandaohu is a monomictic lake with thermal
282 stratification for most of the year, and the temperature gradient shift caused by the
283 default lake scheme or a uniform initial profile cannot be easily corrected during
284 model integration (Perroud et al., 2009). In this study, a straightforward and
285 generalized method was proposed to assign initial values for lake temperature. WRF-
286 Lake was modified to import lake water temperature profiles directly from external
287 files and interpolate them onto the lake grid of the WRF model. We first replaced the
288 lake depths in WRF with the observed bathymetry data. During the model
289 initialization, each water column at lake grids will be discretized into ten layers
290 according to their lake depths. Then we linearly interpolated the temperature profile at
291 Daba to all grids to generate initial conditions for the entire simulation domain. This
292 procedure assumes that the water temperature in Lake Qiandaohu is horizontally
293 homogenous. The measurement depths at Daba are also adequate for providing water
294 temperature profiles for other lake grids. The soil temperature was set equal to the
295 lake water temperature of the bottom layer to ensure that the sediment heat flux was
296 initially zero. Figure 2a depicts the default initial lake water temperature profile in
297 WRF-Lake, observed values, and modified initial lake water temperature profile at the

298 Daba station (0000 UTC on 1st March 2016).

299 **2.4.2. Time-dependent light extinction coefficient**

300 The light extinction coefficient describes the rate at which the incident shortwave
301 radiation is attenuated by lake water, which determines the vertical distribution of
302 solar radiation. In the default WRF-Lake model, the light extinction coefficient was
303 calculated as a function of lake depth (Section 2.3.1) using in situ observations from
304 88 Swedish lakes, which cannot be generalized to global lakes (Subin et al., 2012).
305 The light extinction coefficient at the Daba station, for example, varies between 0.3–
306 0.6 throughout the year, with the highest values in spring and summer; however, the
307 default values in WRF-Lake remain constant and understated (Figure 2b). Therefore,
308 the in situ observed monthly light extinction coefficients of Lake Qiandaohu were
309 taken as model inputs and disaggregated to daily resolution during the simulation
310 period, which accounted for the temporal variability of the light extinction coefficient.



311 Figure 2. (a) Initial water temperature profile at Daba station from the observations,
312 default, and modified lake scheme; (b) Monthly light extinction coefficients from
313

314 sampling and daily light extinction coefficients from the default and modified lake
315 scheme.

316 **2.4.3. Eddy diffusion coefficient**

317 The governing equation of the heat transfer in the WRF-Lake was controlled by
318 molecular diffusion and eddy diffusion. Gu et al. (2015) proved that the model
319 performance for lake temperature was sensitive to eddy diffusion and could be
320 improved by enlarging the eddy diffusivity (k_e) for deep lakes. The default lake
321 model increased k_e by a factor of 100 when the depth of the lake grid exceeded 15 m.
322 In this study, the factor was enlarged to 10^4 and restricted the total heat diffusion
323 coefficient ($k_m + k_e$) with a maximum value of $0.01 \text{ m}^2 \text{ s}^{-1}$ to avoid unrealistic large
324 diffusivity that may occur at the lake surface. This criterion is the largest vertical heat
325 diffusivity observed in the open seas, as suggested by Wang et al. (2019).

326 **2.4.4. Surface roughness lengths parameterization**

327 The surface roughness length of momentum, sensible heat, and latent heat for
328 unfrozen lakes is defined as 0.001 m in the default WRF-Lake, which can be
329 considered excessive for lakes. The method proposed by Subin et al. (2012) was
330 adopted in this study. It calculates the surface roughness lengths based on the friction
331 velocity, fetch, and wind speed as follows:

$$\begin{aligned} z_{0m} &= \max\left(\frac{0.1v}{u_*}, \alpha \frac{u_*^2}{g}\right) \geq 10^{-5} \text{m}, \\ z_{0h} &= z_{0m} \exp\left\{-\frac{\kappa}{Pr} (4\sqrt{R_0} - 3.2)\right\} \geq 10^{-5} \text{m}, \\ z_{0q} &= z_{0m} \exp\left\{-\frac{\kappa}{Sc} (4\sqrt{R_0} - 4.2)\right\} \geq 10^{-5} \text{m}, \end{aligned} \quad (10)$$

333 where ν is the kinematic viscosity of air ($\text{m}^2 \text{s}^{-1}$), u_* is the friction velocity (m s^{-1}), α
334 is the effective Charnock coefficient (given below), $R_0 = \max(\frac{z_0 m u_*}{\nu}, 0.1)$ is the
335 near-surface atmospheric roughness Reynolds number, $P_r = 0.71$ is the molecular
336 Prandtl number for air, and $S_c = 0.66$ is the molecular Schmidt number for water in
337 the air.

338 The Charnock coefficient is defined as follows:

$$\begin{aligned}
\alpha &= \alpha_{min} + (\alpha_{max} - \alpha_{min}) \exp[-\min(A, B)] \\
A &= \left(\frac{Fg}{u_*^2}\right)^{1/3} / f_c \\
B &= \epsilon \frac{\sqrt{dg}}{u}
\end{aligned} \tag{11}$$

340 where $\alpha_{min} = 0.01$; $\alpha_{max} = 0.11$; F is the lake fetch (m); and f_c was set to 22, which
341 corresponds to the use of u_* instead of u when calculating A (Wang et al., 2019); $\epsilon =$
342 1. The fixed-point iteration method proposed by Wang et al. (2019) was also used to
343 update surface roughness lengths and u_* simultaneously.

344 2.5. Datasets

345 2.5.1. Reanalysis datasets

346 The initial and boundary conditions of the WRF model were provided by the 6-
347 hourly ERA5 reanalysis (Hersbach et al., 2020) data with 1° spatial resolution. This is
348 the latest fifth generation of atmospheric reanalysis dataset produced by the European
349 Center for Medium-Range Weather Forecasts and has been applied widely in lake
350 research (<https://www.ecmwf.int/en/forecasts/datasets/reanalysis-datasets/era5>).

351 The China Meteorological Forcing Dataset (CMFD) is a gridded near-surface
352 meteorological dataset with a 0.1° spatial resolution and a three hour temporal

353 resolution (<https://data.tpdc.ac.cn/en/data/8028b944-daaa-4511-8769-965612652c49>).

354 It is developed by combining remote sensing data, reanalysis datasets, and in situ

355 measurements (He et al., 2020; Yang et al., 2010). It has been widely used in other

356 lake modeling studies in China (Wang et al., 2019; Wu et al., 2020). Downward

357 shortwave radiation and longwave radiation from this dataset were used as references

358 to check the performance of the WRF model since the Chun'an weather station does

359 not observe radiation components. CMFD has been used as a representative of

360 observation for assessing other forcing data (Qi et al., 2022); its shortwave radiation

361 has also been proven to be reliable for China (Yang et al., 2017). Despite that, some

362 studies in Lake Namco have found inconsistencies between CMFD and in situ

363 observations (Huang et al., 2019; Shi et al., 2022; Wu et al., 2021). To reduce the

364 uncertainties caused by single forcing data, we also included the ERA5 reanalysis as a

365 reference when validating the simulated longwave and shortwave radiations.

366 **2.5.2 Meteorological observation**

367 Daily observations of meteorological variables, including 2-m temperature, 10-m

368 wind speed, and precipitation at the Chun'an weather station (29.62 °N, 119.02 °E)

369 during 2016, were applied to evaluate the performance of the WRF model in

370 simulating near-surface variables. Data were downloaded from the China

371 Meteorological Data Service Center (<http://data.cma.cn>).

372 **2.5.3 Lake water temperature observation in Lake Qiandaohu**

373 In-situ lake water temperature measurements at the Daba buoy station in 2016

374 (29.51 °N, 119.21 °E; hereafter referred to as “Daba”) are used to calibrate model
375 parameters. The water temperature was recorded every three hours by a
376 multiparameter water-column profiler attached to a buoy. Vertical depths ($\pm 0.005\%$)
377 and water temperature ($\pm 0.002\%$) were sampled at 0.5 m intervals between 0.1–10 m,
378 and 2 m depth increments were used below 10 m (Liu et al., 2019). This sampling
379 location had a maximum depth of 93 m. But the records only reached 65 m because
380 the water temperature is vertically homogenous down below (Liu et al., 2019). For the
381 convenience of cross-comparison, the water temperature from both in situ
382 observations and numerical experiments was interpolated to 0.5 m intervals from 0.5–
383 64 m.

384 **2.5.4. Light extinction coefficient measurements**

385 Light extinction coefficients η (m^{-1}) were obtained from monthly sampling of
386 water transparency z_{secchi} (m) measured by the Secchi disk method. In this study,
387 light attenuation was calculated using the relationship $\eta = 1.3809z_{secchi}^{-0.92}$, which was
388 estimated from a series of concurrent observations of z_{secchi} and light absorption
389 (Figure S5).

390 **2.6. Metrics of stratification and mixing**

391 The lake analyzer (<https://gleon.org/research/projects/lake-analyzer>) is a
392 numerical code package for calculating the key metrics of lake physical states from
393 water temperature, lake bathymetry, and near-surface wind speed (Read et al., 2011).
394 Three indicators were selected to represent the lake thermal structure characteristics

395 during stratification: the thermocline depth (thermD), thickness of the metalimnion
396 (metaTh), and bottom depth of the metalimnion (metaB). ThermD was defined as the
397 depth of the maximum change in water density. The metalimnion range is defined as
398 the water layer where the vertical temperature gradient is $\geq 0.2 \text{ }^\circ\text{C m}^{-1}$ (Liu et al., 2019;
399 Zhang et al., 2014). Schmidt stability, which denotes the resistance of mechanical
400 mixing because of potential energy, was also calculated to represent the temporal
401 variation of lake thermal stability (Schmidt, 1928). The lake number and Wedderburn
402 number were calculated to describe the dynamic stability. The two dimensionless
403 metrics are expressed as the balance of wind stress and the stratified condition. Lake
404 number represents the potential for nonlinear internal waves caused by wind forcing
405 (Imberger and Patterson, 1989). Meanwhile, the Wedderburn number, represents the
406 possibility of upward movement in the metalimnion (Thompson, 1980). Lower lake
407 number and Wedderburn number values indicate a higher likelihood of mixing events
408 (Read et al., 2011).

409

410 **2.7. Experimental design and post processing**

411 Six numerical experiments were conducted to assess the impact of key
412 parameters that individually affect the lake thermal structure and evaluate
413 performance of the modified WRF-Lake model, as shown in the table below. Since
414 lake temperature measurements below 30 m were not available from January to
415 February 2016, all simulations ran from March 1, 2016, to January 1, 2017, and the

416 first 20 days were discarded as model spin-up.

417 Table 1. Model parameter setting for different cases.

Case	Description
CTL	Control experiment
INI	Modified initial lake temperature as described in Section 2.4.1
KD	Modified lake light extinction coefficient as described in Section 2.4.2
KE	Modified eddy diffusivity as described in Section 2.4.3
Z0MG	Modified surface roughness lengths as described in Section 2.4.4
MOD	Calibrated model based on INI, KD, KE, and Z0MG

418 In this study, the mean bias error (MBE) was used to represent systematic error
419 of the lake model. This metric provides the average bias of a model in comparison to
420 observations and indicates whether the model needs to be corrected. The root mean
421 square error (RMSE) was used to assess the credibility of the model. This is the
422 standard deviation of the predicted errors and is highly sensitive to the most
423 significant errors.

424

425 **3. Results**

426 In this section, the results from the WRF-Lake simulations are first validated
427 using in situ observations and other available datasets. After the sensitivity
428 experiments, the lake water temperature and the sensible and latent heat fluxes are
429 further analyzed to determine the effects of key model parameters on the lake surface
430 energy balance and thermal structure.

431 **3.1. Model validation**

432 3.1.1 Comparison of meteorological variables

433 The simulated near-surface air temperature and wind speed from the control
434 experiment were compared with those obtained from meteorological observations.
435 Since radiation measurements from nearby weather stations were unavailable, the
436 CMFD dataset was used as a reference to assess the accuracy of downward shortwave
437 and longwave radiation, which act as the primary energy sources for the lake.

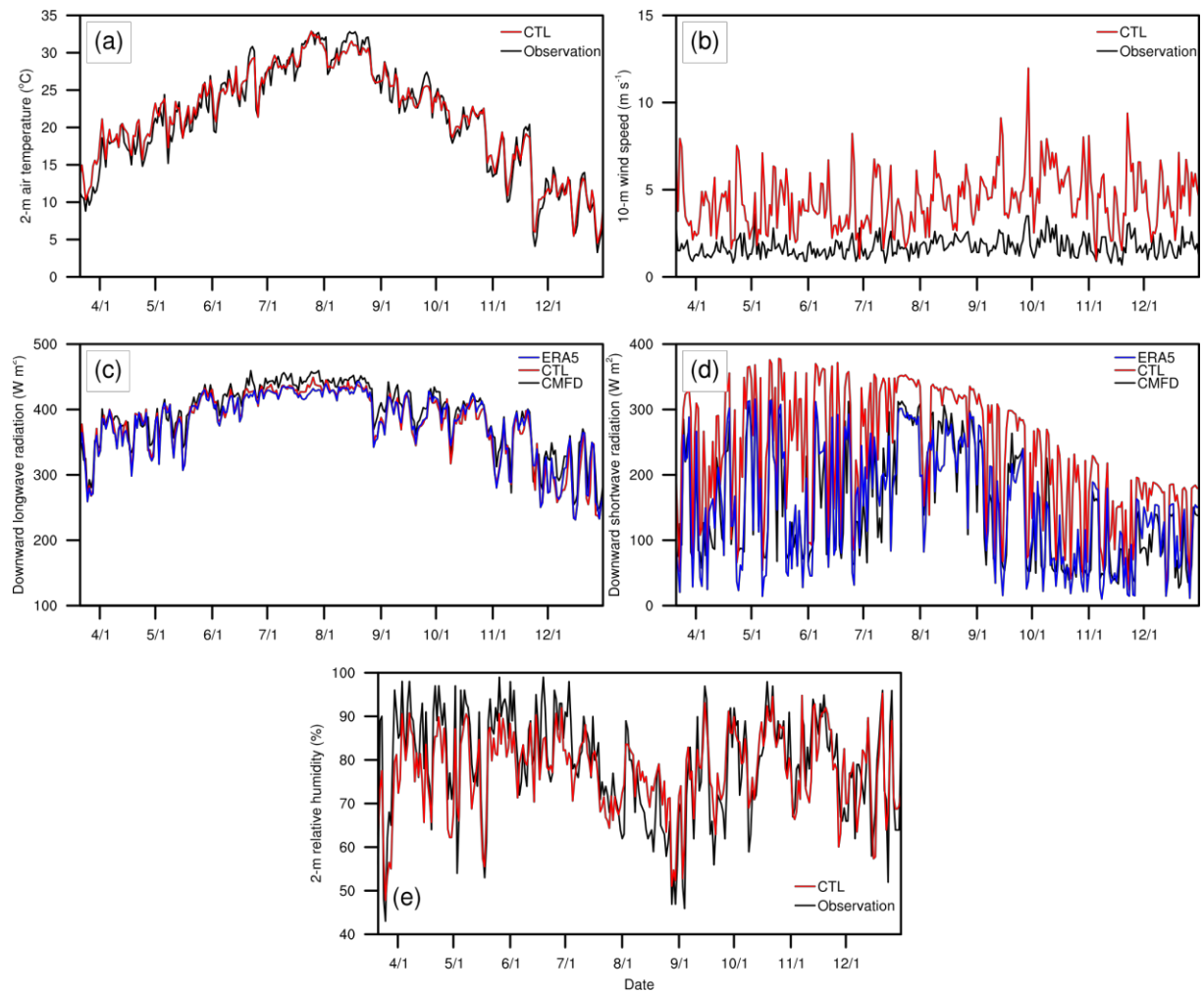
438 The WRF model accurately reproduced daily variations of 2-m air temperature,
439 downward longwave radiation, and 2-m relative humidity, as well as the seasonal
440 pattern of downward shortwave radiation and 10-m wind speed (Figure 3). The
441 comparison of simulated spatial pattern between CTL and reanalysis dataset were
442 shown in Figure S13-14. As shown in Figure 3 and Table 2, the temporal variations in
443 air temperature and downward longwave radiation were captured well by the WRF
444 with an MBE of 0.4 °C (- 0.6/-13.9 W m⁻²; the comparison between WRF and
445 ERA5/CMFD) and a RMSE of 1.3 °C (9.3/20.4 W m⁻²). The WRF model
446 underestimated relative humidity by an MBE of -1.5%. This is possibly related to the
447 warm biases in air temperature, which results in larger saturated water vapor pressure.
448 The WRF model was also able to simulate reasonably the daily variation in wind
449 speed, although there is a large positive bias with an annual MBE of 2.7 m s⁻¹ and an
450 RMSE of 3.0 m s⁻¹. This indicates a systematic overprediction of wind speed and the
451 degree of which amplified at higher velocities. The simulated downward shortwave
452 radiation was also overestimated, with a mean MBE of 82.0/84.7 W m⁻². Detailed

453 investigations of the overprediction of wind speed and shortwave radiation are not
 454 within the scope of this study. However, their effects on lake thermal structures are
 455 further discussed in Section 4.1.

456 Table 2. Annual mean bias error (MBE) and root mean square error (RMSE) of the
 457 WRF model simulation when compared with the observations (2-m air temperature,
 458 10-m wind speed, and 2-m relative humidity) and reanalysis dataset (downward
 459 shortwave and longwave radiation).

	Reference data	MBE	RMSE
2-m air temperature (°C)	in situ	0.4	1.3
10-m wind speed (m s ⁻¹)	in situ	2.7	3.0
Downward longwave radiation (W m ⁻²)	ERA5 CMFD	-0.6 -13.9	9.3 20.4
Downward shortwave radiation (W m ⁻²)	ERA5 CMFD	82.0 84.7	95.8 103.0
2-m relative humidity (%)	in situ	-1.5	7.0

460



461

462 Figure 3. Daily variations in (a) 2-m air temperature ($^{\circ}\text{C}$), (b) 10-m wind speed (m s^{-1}),

463 (c) downward longwave radiation (W m^{-2}), (d) downward shortwave radiation (W m^{-2}), and (e) 2-m relative humidity (%).

464 Air temperature, wind speed, and relative

465 humidity are compared to the observations from the Chun'an weather station.

466 Longwave and shortwave radiation are compared with those obtained from reanalysis

467 datasets (i.e., CMFD and ERA5). All variables were interpolated from model grid

468 cells to the Chun'an station.

469

470 3.1.2 Comparison of lake surface energy processes

471 LSWT is determined by heat exchange processes at the air–water interface,

472 namely, absorbed radiation, heat conduction, and heat loss by evaporation (Edinger et
473 al., 1968). Since the net shortwave radiation and downward longwave radiation are
474 subjected to atmospheric conditions, this section analyzes the LSWT and turbulent
475 fluxes to determine effects of the model parameters on the lake surface energy
476 processes. The emitted longwave radiation is not included because it is proportional to
477 the fourth power of the absolute temperature (the first term on the right-hand side of
478 Eqn. 3); thus, it varies naturally with LSWT.

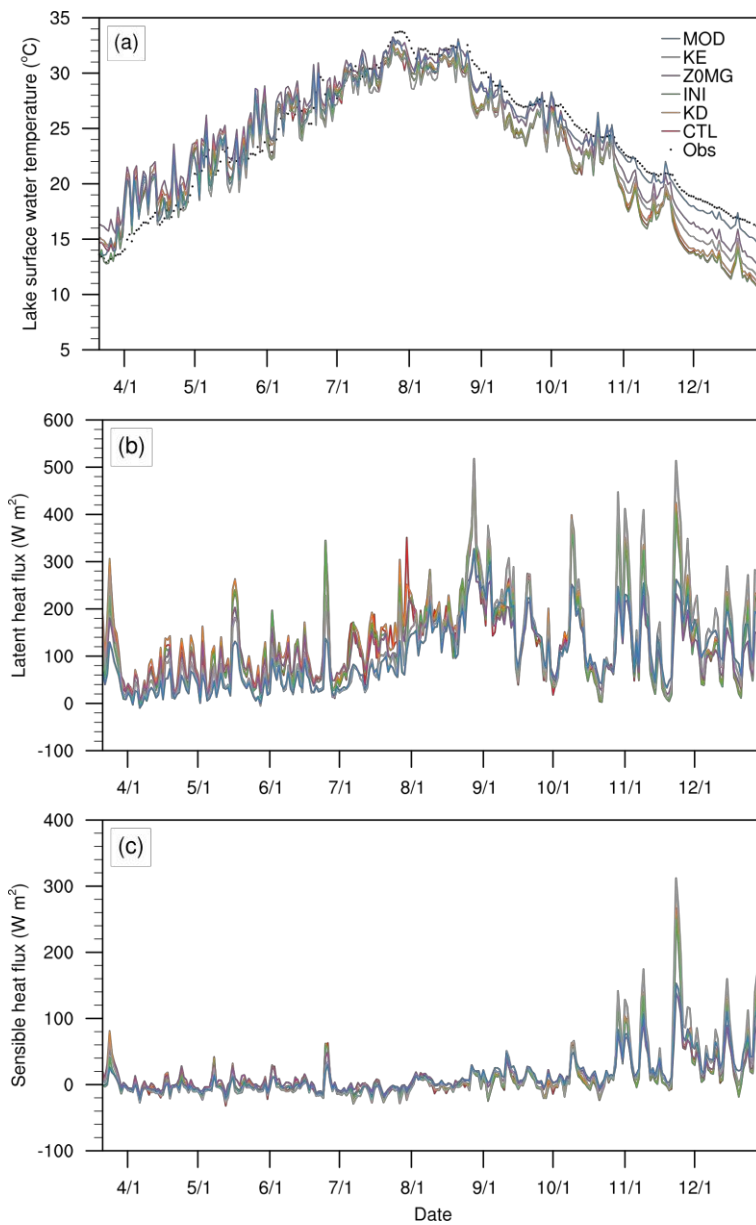
479 LSWT in this study is the average water temperature between 0-2 m. The
480 simulated data at 0400 UTC (12:00 in local time) each day were chosen for a stable
481 and intense thermal stratification (Liu et al., 2019). The WRF-Lake results were
482 interpolated to the location of Daba buoy to compare with the observations. Results of
483 simulated LSWT, sensible and latent heat are shown in Figure 4 and Figure S6. The
484 comparison of simulated spatial pattern between CTL and other experiments of lake
485 water temperature at the top model layer was shown in Figure S15. Compared with in
486 situ data, CTL successfully reproduced the seasonal variation of water temperature
487 (Figure 4a), but significantly underestimated LSWT from September to December.
488 This results in an annual MBE of -1.3 °C, which indicates a systematic cold bias. In
489 addition, CTL simulated excessive variation in LSWT, particularly during the
490 warming period (March–June), with an average of 1.7 °C. It is still comparable to the
491 daily variation in air temperature (1.7 °C) but considerably higher than the observed
492 daily variation in water temperature (0.5 °C).

493 CTL generated a reasonable temporal pattern of turbulent heat fluxes at the lake
494 surface. Figure 4b shows that the latent heat flux exhibited an increasing trend before
495 September and reached its peak in autumn because of the lag between the LSWT and
496 air temperature (Schmid and Read, 2021). This is consistent with the enhanced
497 sensible heat flux since August (Figure 4c) and implies that the lake surface is warmer
498 than the overlying atmosphere and serves as a heat source. Figures 4b and 4c also
499 highlight the dominant contribution of evaporation to turbulent heat fluxes, as is
500 expected in low-latitude lakes such as Lake Qiandaohu (Woolway et al., 2018).

501 As indicated by the RMSE and MBE (Figure 5), all five parameter sensitivity
502 experiments improved the accuracy of LSWT except INI, which exacerbated the cold
503 biases. Results with increased light extinction coefficient warmed the water surface
504 during most of the simulation period (93.4%), consequently yielding a 0.4 °C increase
505 in annual MBE. The INI experiment corrected the overestimation of LSWT at the
506 beginning of the simulation. The difference between INI and CTL diminished until
507 November, when INI began to display a negative bias against CTL and eventually
508 resulted in a decrease in annual MBE of 0.1 °C. The only experiment with a positive
509 MBE of 0.1 °C against observation was Z0MG. This matched the minimum latent
510 heat flux generated by Z0MG in the five sensitivity experiments (Figure 4b). Despite
511 an increase of 1.1 W m⁻² in the annual average sensible heat flux of Z0MG, the latent
512 heat flux decreased by 14.0 W m⁻² because of less effective moisture exchange at the
513 air–water interface and dominated changes in LSWT. Enlarging the eddy diffusivity in

514 the deep layers mitigated the cold bias of the LSWT from October to December,
515 which was analogous to Z0MG. However, for the other months of the year, KE
516 estimated colder LSWT than CTL.

517 After the calibrations, the MOD experiment achieved a minimum MBE of $-0.1\text{ }^{\circ}\text{C}$
518 and lowered the RMSE from $2.9\text{ }^{\circ}\text{C}$ to $1.6\text{ }^{\circ}\text{C}$. The remaining cold bias was partially
519 because of the positive bias in the near-surface wind speed introduced by the WRF
520 model (Figure 3b). Windier conditions promote stronger mixing events in the
521 epilimnion and favor turbulent heat loss (especially latent heat) at the air–water
522 interface, thereby resulting in a cooling effect on LSWT (Woolway et al., 2018).

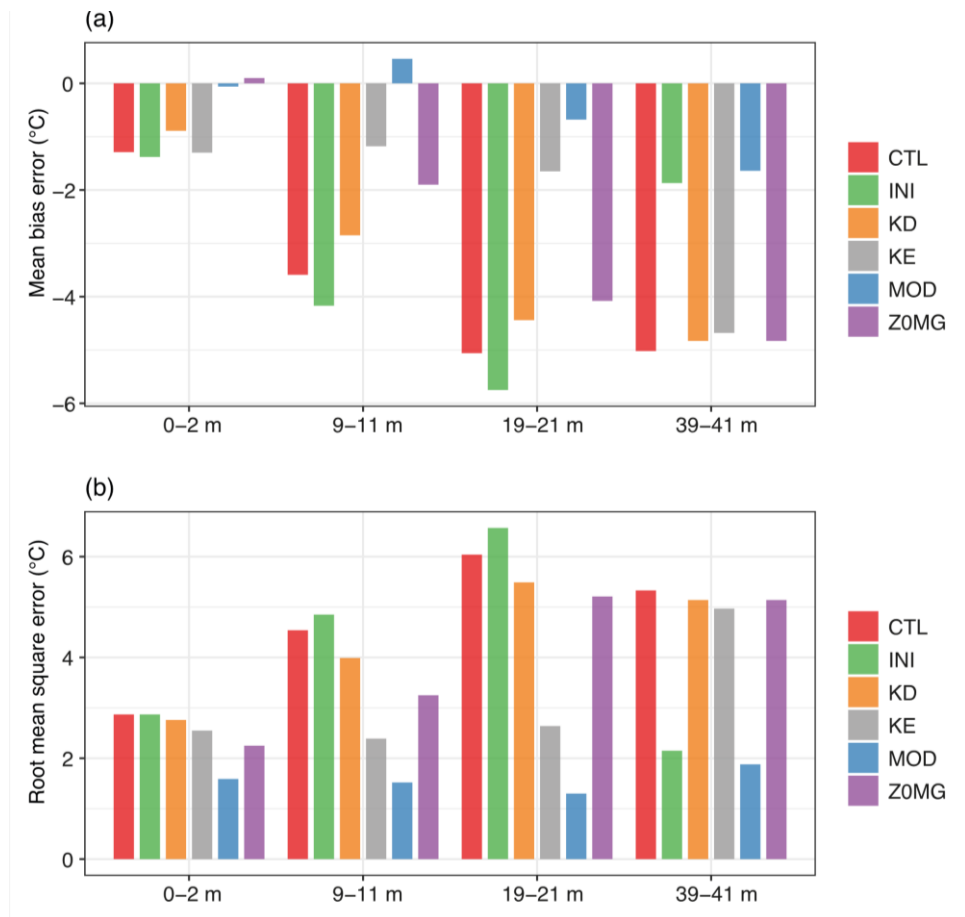


523

524 Figure 4. Daily variation of (a) lake surface water temperature ($^{\circ}C$), (b) sensible heat

525 flux ($W m^{-2}$), and (c) latent heat flux ($W m^{-2}$)

526



527

528 Figure 5. (a) Mean bias error (°C) and (b) root mean square error (°C) for 0–2 m, 9–
 529 11m, 19–21 m, and 39–41 m averaged water temperature between the simulation
 530 results and observations.

531 3.2. Simulating stratification in Lake Qiandaohu

532 Results of the CTL experiment showed that the original lake scheme could
 533 represent the temporal evolution of lake stratification. Lake thermal stratification
 534 began in March and strengthened rapidly in April, with the temperature difference
 535 between the surface and bottom of the lake (hereafter denoted as T_{diff}) exceeding 5 °C
 536 on April 2. Further, lake stratification was found to be strongest during summer, when
 537 the temperature difference reached 23.4 °C on July 26 (Figure 6a). CTL captured this
 538 feature relatively well, with the maximum temperature difference occurring on July

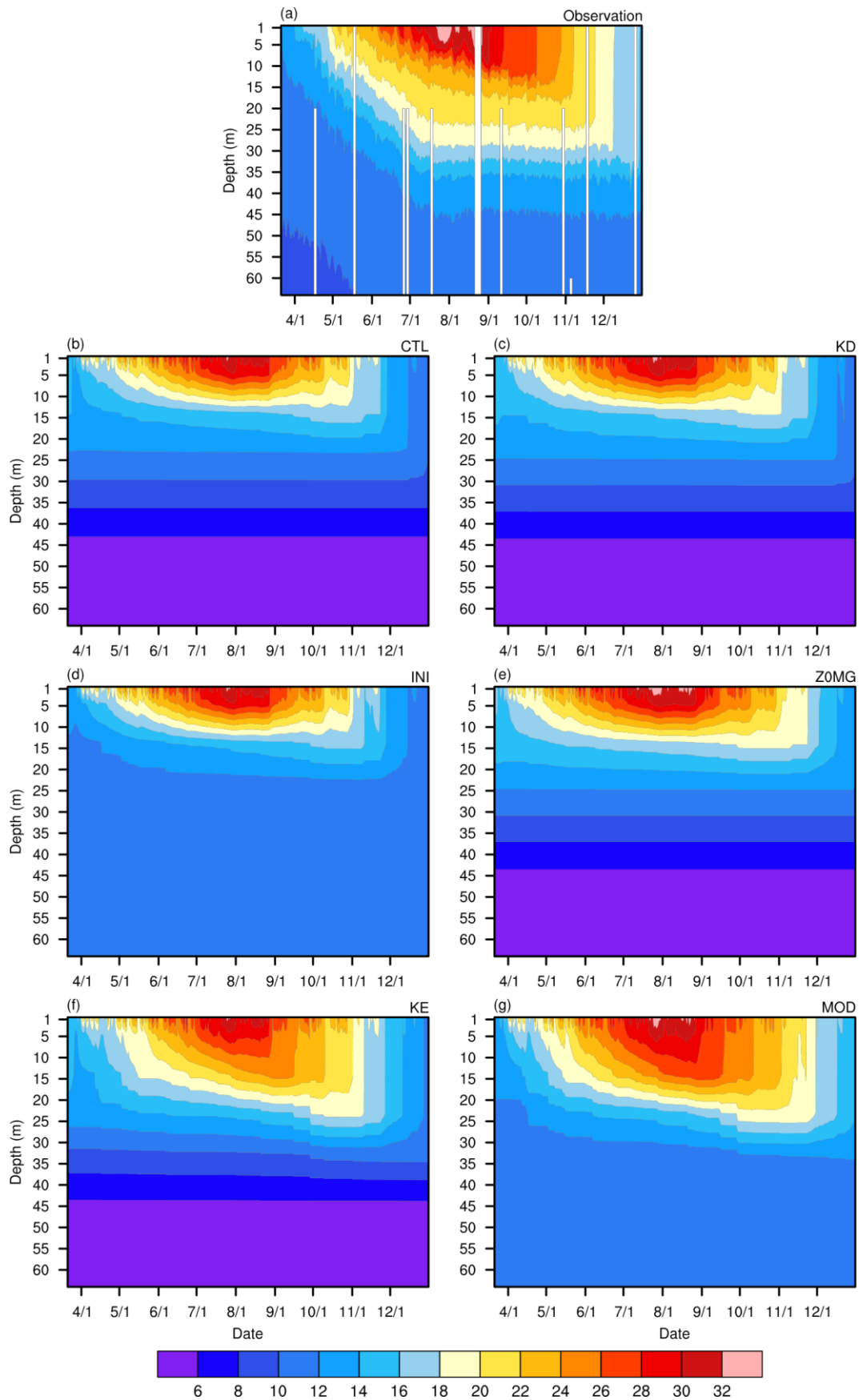
539 25 (Figure 6b). However, CTL predicted an earlier spring warm-up and autumn cool-
540 down. The hypolimnion temperature was severely underestimated, which results in an
541 unrealistic vertical temperature gradient in the deep layers. This also caused the
542 maximum T_{diff} of the CTL experiment to be 6 °C higher than that observed. Moreover,
543 the default lake scheme generated weaker lake stratification, which is indicated by the
544 negative annual MBE of the thickness of the metalimnion in the INI experiment
545 (Figure 10). It is noteworthy that the positive systematic error of the metalimnion
546 bottom depth and metalimnion thickness in CTL was attributable to overestimation of
547 the initial hypolimnion temperatures.

548 As shown in Figure 6, the lake temperature simulated by KD and Z0MG were
549 very close to that of CTL. Although the hypolimnion temperature in the INI
550 experiment was more accurate, it simulated a metalimnion structure that was very
551 similar to that of CTL, which was greatly improved in the KE experiment. These
552 results confirm that the vertical heat distribution is primarily governed by the mixing
553 process (Subin et al., 2012). Modifying surface properties of the lake (such as surface
554 roughness lengths and light extinction coefficient) has limited effects on the vertical
555 temperature pattern (Xiao et al., 2016).

556 Figure 7 and Figure S10 showed the differences in the temperature simulated
557 from all the sensitivity experiments against CTL and the observations, respectively.
558 The comparison of vertical water temperature profile was depicted in Figure S11. It
559 can be first noted that the KD and Z0MG were both close to CTL and showed an

560 overall warming trend in the whole water column. INI and KE showed the largest
561 deviation from CTL. An increase in the light extinction coefficient resulted in a
562 warming of the lake surface in early summer, as well as a water temperature of
563 approximately 15 m during stratification, leading to a temperature increase of 2.0 °C.
564 Negative values only occurred at the lake surface for a few days, possibly because of
565 the increased latent heat flux (Figure 4c). The INI experiment removed cold bias
566 below 25 m. However, it tends to produce a warmer LSWT from June to October and
567 a colder metalimnion throughout the year, deteriorating the model performance at 9–
568 11 and 19–21 m (Figure 5). When a parameterization for surface roughness lengths
569 was used, the water column temperature increased by an average of 0.6 °C above 25 m.
570 The most pronounced improvements occur at 1–15 m in winter, which largely delayed
571 the earlier prediction of the autumn cool-down, although an even earlier warm-up was
572 estimated (Figure 6e). Enlarging the eddy diffusivity decreased the water temperature
573 above 5 m before September and increased the water temperature below it, thereby
574 implying that more heat energy was transferred to the deep layers by enhancing the
575 mixing strength. Warmer deep layers allow more energy to be stored below the mixed
576 layer, where the air–water heat exchange takes place. This further enhances the
577 resistance of the lake to declining air temperature, which is indicated by the warmer
578 water column in winter. These results suggested that, in addition to dominating the
579 development of the metalimnion, the mixing strength in the lake model influences the
580 thermal structure during the subsequent cool-down period. We have also performed a

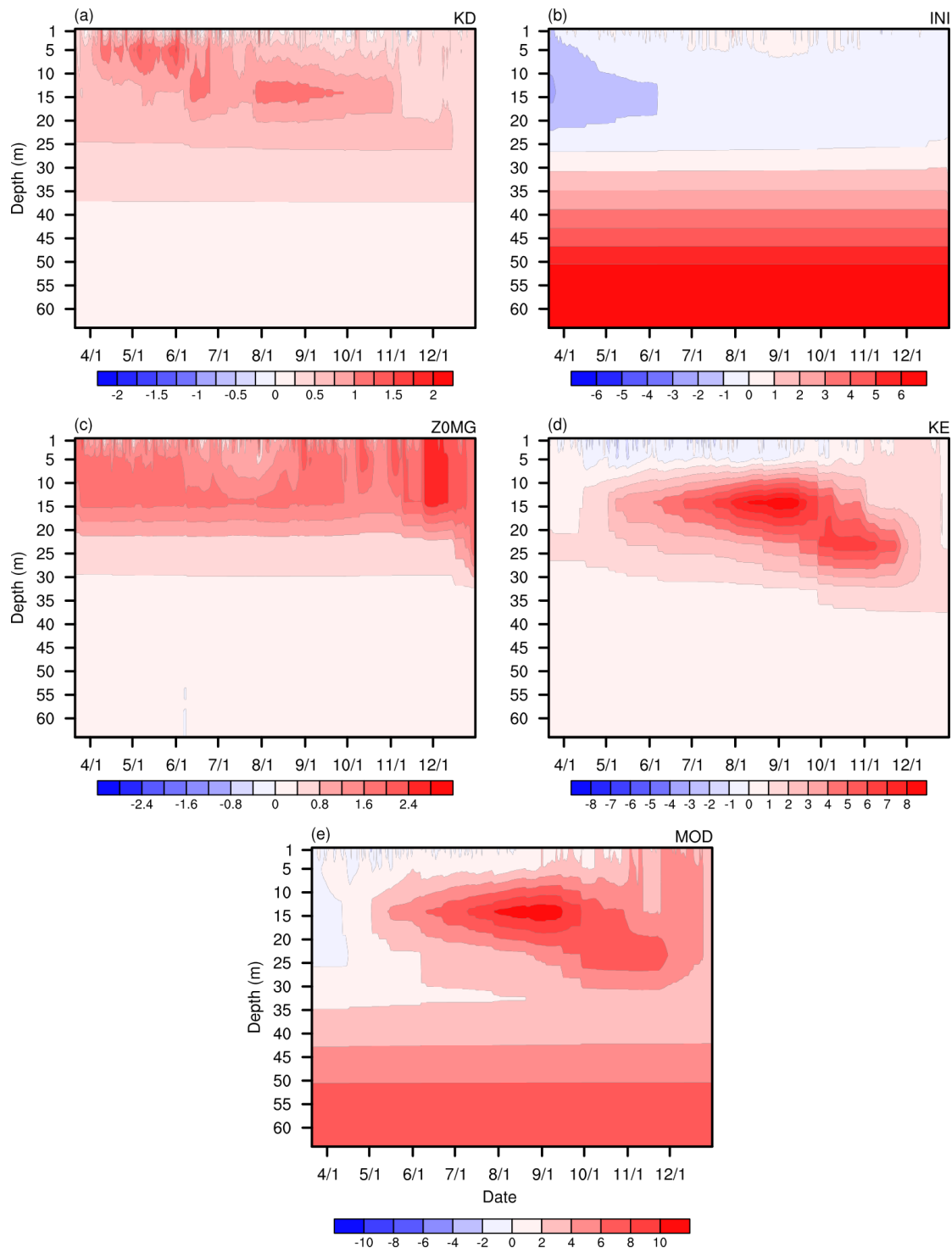
581 numerical experiment with only the modified initial water temperature profile and
582 eddy diffusivity (Figure S16 and Table S3). The results produced a similar thermal
583 structure with MOD, but the water temperatures above 25 m were colder and showed
584 larger biases. This suggests that the initial water temperature profile and eddy
585 diffusivity were most critical for simulating the evolution of the lake thermal structure.
586 At the same time, modifying light extinction coefficients and surface roughness
587 lengths, which mainly increased water temperature in shallow layers, are important as
588 well.
589



590

591 Figure 6. Lake water temperatures (°C) at the Daba station in 2016 (a) from

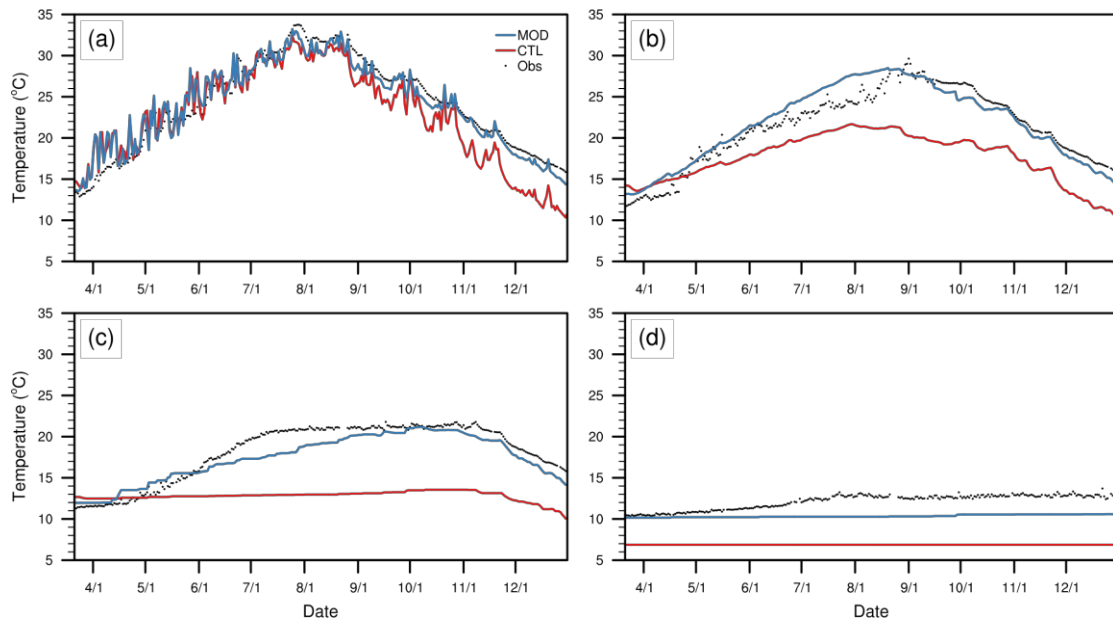
592 observations and as predicted by the lake models: (b) CTL, (c) KD, (d) INI, (e) Z0MG,
593 (f) KE, (g) MOD.



594
595 Figure 7. Differences between lake water temperatures ($^{\circ}\text{C}$) simulated by (a) KD, (b)
596 INI, (c) Z0MG, (d) KE, and (e) MOD and CTL.

597

598 The performance of the MOD experiment in simulating water temperature at
599 certain depths is shown in Figure 8. Figure 8 b–d denotes the water temperature at a
600 depth of 9–11 m (above the thermocline), 19–21 m (below the thermocline), and 39–
601 41 m (hypolimnion), respectively. In summary, accuracy of the lake scheme was
602 greatly improved by modifying the aforementioned key model parameters, namely,
603 the initial lake water temperature, light extinction coefficient, eddy diffusion
604 coefficient and surface roughness lengths. The MOD experiment captured the
605 seasonal variation and magnitudes of water temperature and reproduced the extended
606 highest water temperature at 19–21 m compared to that at the surface. Nevertheless,
607 the differences between the MOD and in situ measurements became apparent as the
608 depth increased. Overestimation of water temperature at 9–11 m from June to August
609 and underestimation in 19–21 m suggests insufficient heat transfer below the
610 thermocline. The MOD experiment also failed to reproduce the slow warm-up of the
611 hypolimnion temperatures, thereby implying unresolved mixing processes in the deep
612 layers.

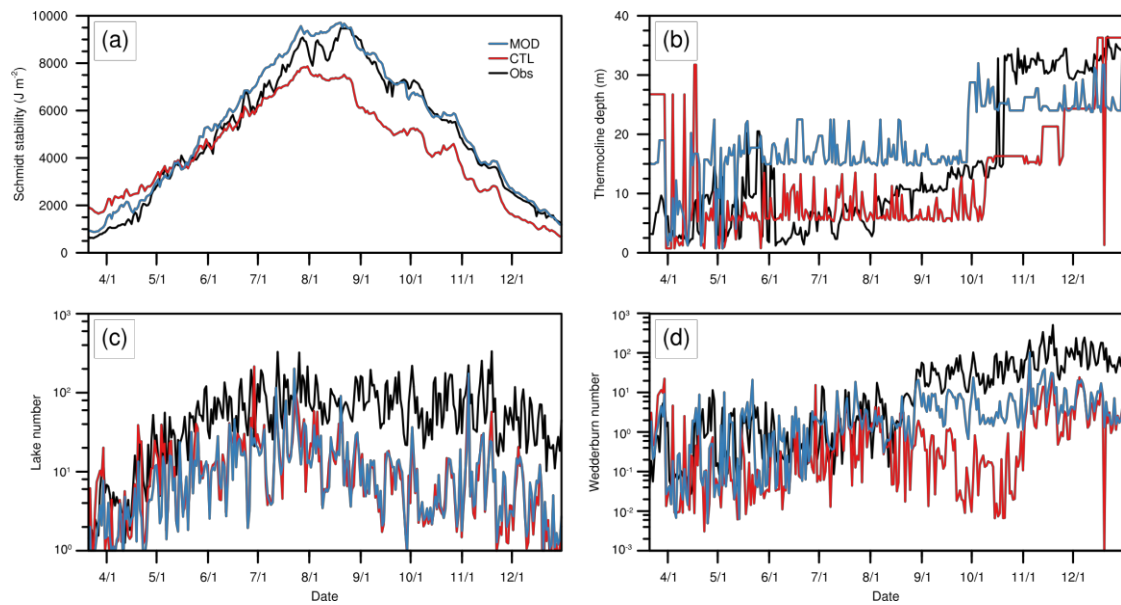


613
 614 Figure 8. Temporal variation of daily water temperature (°C) at depths of (a) 0–2 m, (b)
 615 9–11 m, (c) 19–21 m, and (d) 39–41 m from CTL and MOD simulations and in situ
 616 observations.

617

618 The temporal variations in the four modelled lake stability indicators calculated
 619 by Lake Analyzer were consistent with those calculated from the observations (Figure
 620 9). Schmidt stability varies coherently with LSWT as it only depends on the water
 621 density (Figure 9a). The rising Schmidt stability before September suggested that the
 622 kinetic energy required to disturb lake stratification increased. Thermal stability
 623 weakened during the cooling period but still exceeded 1000 J m^{-2} in winter, which is
 624 reasonable for a deep and warm monomictic lake. The magnitude of the Schmidt
 625 stability in the MOD experiment was consistent with that of the observations, which
 626 was attributed to a better representation of the vertical heat content. Figure 9b shows
 627 that the thermocline depth changed rapidly in spring and gradually deepened with a

628 strengthening of summer stratification. During the cool-down period, the upper water
629 column was fully mixed, and the thermocline depth was maintained near the bottom
630 of the metalimnion. The MOD and CTL experiments both captured the sudden
631 increase in thermocline depth in autumn, but failed to reproduce the steady growth
632 behavior before that. The overestimation of wind speed and hypolimnetic water
633 density resulted in lower lake numbers in the numerical experiments (Figure 9c). The
634 lake number from the observations increased with Schmidt stability and the bottom
635 layer depth of the metalimnion from April to July and then slowly decreased. For
636 most of the year, the lake number from the observations remained above 10, which
637 implies that wind forcing could only stir the uppermost layer of the lake and was
638 incapable of diapycnal mixing (MacIntyre et al., 1999). Similar to the lake number,
639 the Wedderburn numbers in the simulations were also underestimated owing to an
640 overestimation of wind speed (Figure 9d). Variations in the Wedderburn number were
641 primarily determined by changes in the mixed layer depth. In the CTL experiment, the
642 mixed layer depth remained stable until November, which caused a downward trend
643 in the Wedderburn number from August to October owing to the reduced density
644 difference between the epilimnion and hypolimnion. However, the Wedderburn
645 number increased with the mixed layer depth since September in the MOD
646 experiment and observations. The Wedderburn number calculated from observations
647 seldom fell below one, which suggests a low likelihood of upwelling events.



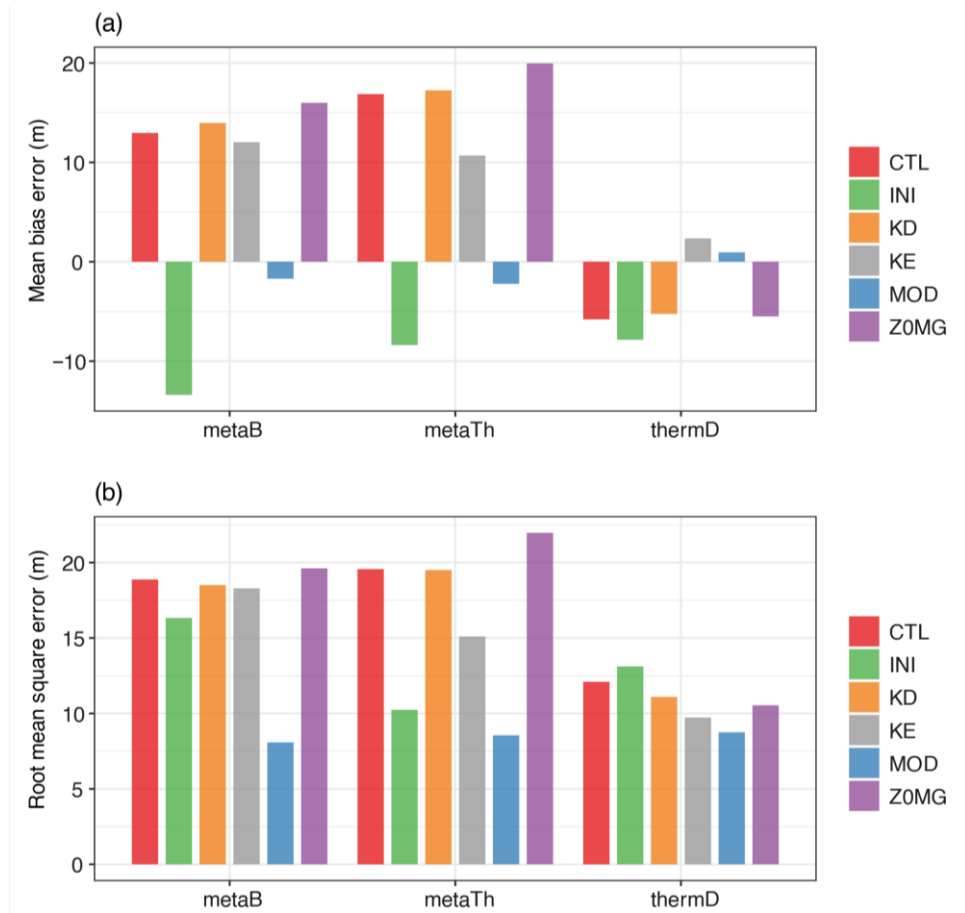
648

649 Figure 9. Temporal variation of daily (a) Schmidt stability ($J m^{-2}$), (b) thermocline
 650 depth (m), (c) lake number and (d) Wedderburn number from CTL and MOD
 651 simulations and in situ observations.

652

653 Figure 10 demonstrates the accuracy of the simulated thermal stratification by
 654 the annual MBE and RMSE of the thermal characteristics in the numerical
 655 experiments against observations. The MOD experiment improved the model
 656 performance in estimating metaTh and metaB and reduced the MBE to -2.2 m and $-$
 657 1.7 m, respectively. The remaining negative biases may be attributed to the weaker
 658 mixing strength below the thermocline (Figure 8 c–d). The ThermD estimated by the
 659 tuned model has an MBE of 1.0 m and an RMSE of 8.8 m, which is significantly
 660 better than that in large-scale simulations with uncalibrated models (Guo et al., 2021).
 661 The MOD experiment also improved the performance of the model in simulating the
 662 strength of summer stratification. The T_{diff} estimated by the MOD was 23.7 °C

663 occurred on July 25, with 0.2 °C higher than that in observations and one day ahead.



664

665 Figure 10. (a) Mean bias error (m) and (b) root mean square error (m) of simulated
666 metalimnion bottom depth (metaB), metalimnion thickness (metaTh), and thermocline
667 depth (thermD) against the observations.

668

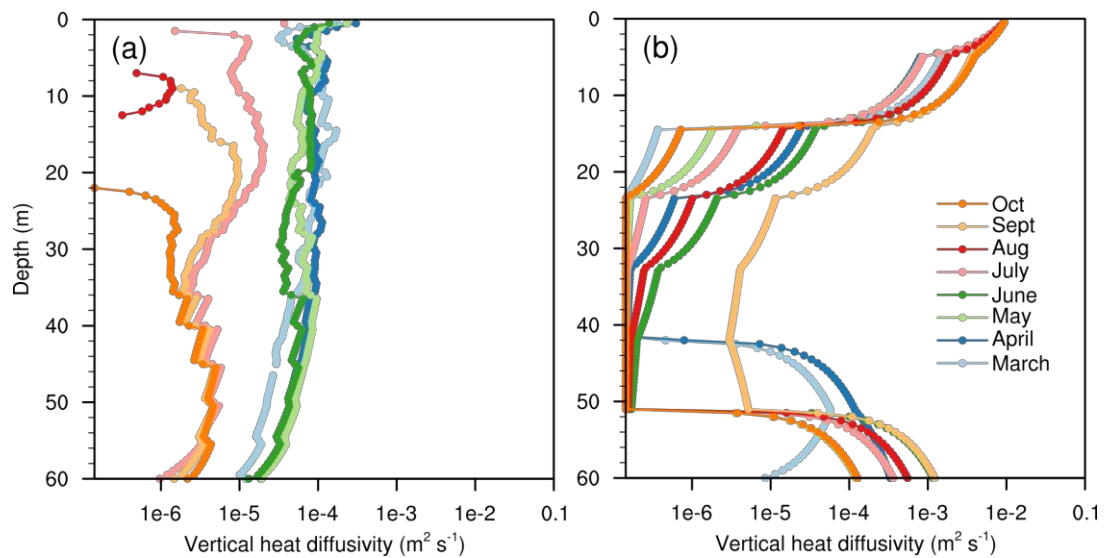
669 3.3. Calculation and analyses of eddy diffusivity

670 k_e was computed from the observed water temperature using the approach
671 described in Section 2.3.2 to quantitatively evaluate the limitation of the Henderson-
672 Sellers eddy diffusivity. It is noteworthy that k_e produced by Eqn. (14) is a proxy for
673 all three-dimensional processes that contribute to turbulence in Lake Qiandaohu.
674 Therefore, a similar variation pattern and magnitude of the tuned k_e were expected for

675 accurate simulation of the thermal structure.

676 Figure 11 depicts k_e computed from the observations (k_{eobs}) and the enlarged k_e
677 in the MOD experiment (k_{emod}). The profiles of k_{emod} at different seasons were very
678 similar. The k_{emod} first decreased markedly with increasing depth and reached its
679 minimum in the 20–50 m depth range because of increasing vertical temperature
680 gradients. Notably, the water temperature at deep layers was almost homogeneous in
681 the vertical direction (Figure 6g; Figure S11), and the R_i in Eqn. (5) decreased from
682 $\sim 10^2$ to zero (Figure S12) and therefore resulted in large k_{emod} comparable to that in
683 shallow layers. This behavior suggests that WRF-Lake is also unable to simulate the
684 vertical heat distribution in the hypolimnion, not only its temporal variation (Figure
685 8d), which is possibly related to the unresolved heat diffusion in the hypolimnion (see
686 discussion in Section 4.2.3). It is evident that the profiles of k_{eobs} varied significantly
687 with time and depth. The k_{eobs} values ranged from 1.3×10^{-8} to $3.0 \times 10^{-4} \text{ m}^2 \text{ s}^{-1}$ with
688 an average of $4.0 \times 10^{-5} \text{ m}^2 \text{ s}^{-1}$. This result is consistent with previous findings in Lake
689 Zurich, another large and deep lake (Li, 1973). The highest k_{eobs} occurred in early
690 summer (March–June), caused by the warming of the water column and the relatively
691 weak vertical temperature gradient. After the stabilization of stratification in summer,
692 the k_{eobs} rapidly declined because of the strong temperature gradient. In August, the
693 k_{eobs} was negative at almost every depth except 7–12.5 m, where the warming trend
694 lasted until September. This phenomenon is in line with the observed lagged
695 maximum temperature in 9–11 m compared to that in 0–2 m from observations

696 (Figure 8a–b). The profiles of k_{eobs} in early summer showed a local minimum of
 697 k_{eobs} at approximately around 2.5 m, which corresponds to the depth of thermocline.
 698 The k_{eobs} further increased and formed a maximum at approximately 20 m. Below 20
 699 m, the behavior of k_{eobs} varied largely with depth in different seasons. In March and
 700 April, k_{eobs} gradually decreases with depth from top to bottom. In the remaining
 701 months, however, the k_{eobs} formed a local minimum at 30–40 m, which is possibly
 702 related to the warm-up of water temperature at 39–41 m (Figure 8d). The minimums
 703 of the k_{eobs} profile matched the two gradient extremes in water temperature profile
 704 (Figure S7).



705
 706 Figure 11. Vertical heat diffusivity ($m^2 s^{-1}$) (a) calculated from water temperature
 707 measurements and (b) simulated by the MOD experiment.

708

709 4. Discussion

710 This study aimed to simulate the temporal evolution of thermal stratification in a
 711 subtropical deep reservoir, Lake Qiandaohu, using an improved WRF-Lake model.

712 The results show that the improved model with the necessary parameterization can
713 capture variations in water temperature and intensity of lake stratification.

714 **4.1. Model uncertainty**

715 In a coupled system, the foremost concern is the error introduced by the
716 atmospheric model (in this case WRF) for simulating physical processes in the lake.
717 The 10-m wind speed and downward shortwave radiation were largely overestimated
718 by the model. The near-surface wind speed of the ERA5 reanalysis, which provided
719 initial and boundary conditions, showed a magnitude comparable to the observations
720 (Figure S8). This overprediction may be related to deficiencies in the WRF model.
721 WRF is deficient in representing the drag effect because of subgrid-scale orography
722 and tends to underestimate wind speed spatial variability over complex terrain
723 (Jiménez and Dudhia, 2012); thus, WRF overpredicts wind speed in valleys, where
724 Lake Qiandaohu is located (Figure 1b).

725 Positive error of the downward shortwave radiation simulated by the WRF model
726 is consistent with previous studies that evaluated the performance of atmospheric
727 models in representing surface energy fluxes. For example, the WRF model
728 overestimated shortwave radiation with an average MBE of 152.9 W m^{-2} compared to
729 those of the hourly observations in the Heihe River Basin (Pan and Li, 2011). The
730 biases of simulated surface insolation is caused by an inaccurate representation of the
731 radiation transfer process between the top of the atmosphere and ground (Wild, 2005).
732 This suggests that misrepresentations of cloud properties, rather than radiation

733 schemes, are responsible for these biases (Jousse et al., 2016). Studies at regional
734 scales have also suggested that an overestimation of the downward shortwave
735 radiation by WRF may be attributable to the lack of cumulus cloud amount and
736 uncertainty in aerosol optical depth (Avolio et al., 2017; Kumar et al., 2015; Ruiz-
737 Arias et al., 2016).

738 In the lake scheme, wind speed was used to calculate the friction velocity, which
739 further influenced the simulated water temperature from two perspectives. First, the
740 sensible and latent fluxes from Eqn. (1) are estimated using the bulk aerodynamic
741 algorithm proposed by Zeng et al. (1998), where the surface fluxes of heat and water
742 vapor are proportional to the friction velocity. Second, the 2-m wind speed in Eqn. (5)
743 also varies with the friction velocity. Therefore, a higher wind speed promotes the
744 efficiency of heat and water vapor exchange at the lake surface and enhances mixing
745 strength in the subsurface (Woolway et al., 2021). Schmid et al. (2014) investigated
746 sensitivity of the lake surface equilibrium temperature to climate forcing variables.
747 According to these findings, overestimation of the average annual 10-m wind speed
748 by 2.7 m s^{-1} (Table 2) will lead to a decrease in LSWT by $2.7 \text{ }^\circ\text{C}$. However, LSWT
749 will simultaneously increase by $2.5\text{--}4.9 \text{ }^\circ\text{C}$ because of positive biases in solar radiation.
750 Therefore, the effects of overestimated wind speed and downward shortwave radiation
751 on LSWT may partially compensate for each other. The remaining cold bias in LSWT
752 is presumably because of the favored turbulent heat loss (especially latent heat) under
753 windy conditions (Woolway et al., 2018). Notably, the enhancement of mixing

754 strength by increased wind speed remains in the modified model and might be
755 amplified as the eddy diffusivity is increased. However, extremes in eddy diffusivity
756 was constrained with a fixed value; thus, it is reasonable to speculate that the
757 influence of high wind speed on the formation of lake thermal stratification was
758 limited. Moreover, our sensitivity analysis using offline WRF-Lake model (see
759 Supporting information 1) suggested that the effect of strong winds is most distinct
760 during autumn, in which the water temperature above 30 m increased, possibly due to
761 deeper mixed layer depth and larger amounts of water participated in the lake-air heat
762 exchange. The enhanced solar radiation increased the water temperature above 20 m
763 (Figure S2), which might increase the strength of lake stratification.

764 The changes in lake surface temperature may also influence the condition of the
765 overlying atmosphere. Generally, lakes could mitigate the regional climate by
766 decreasing the annual range of air temperature and increasing nearby precipitations
767 (Dai et al., 2018b; Wen et al., 2014). Therefore, we compared the temporal variations
768 of simulated near-surface air temperature and daily precipitation in the CTL and MOD
769 experiment as shown in Figure S9. It can be noted first that the MOD experiment has
770 similar seasonal patterns to that of CTL. The warmer lake surface in the MOD
771 experiment heated the overlying atmosphere. This alleviated the underestimation of
772 summer air temperature in CTL but also amplified the overestimation of winter air
773 temperature. The occurrences of rainfall events are consistent in these two
774 experiments. Simulated precipitation in spring is underestimated in both experiments.

775 The most distinct difference existed in May and June, in which the magnitude of
776 precipitation in MOD was even less. This suggests that the volume of Lake
777 Qiandaohu is not large enough to impact atmospheric circulations. Therefore, the
778 improved lake scheme may slightly influence the magnitude of atmospheric variables
779 but cannot change its overall pattern. The effects could be either improvement or
780 deterioration, depending on the original biases of WRF.

781

782 **4.2. Parameter sensitivity**

783 **4.2.1. Time-dependent light extinction coefficient**

784 It has been described that darker surface waters tend to form shallower mixed
785 layers owing to the less deeply penetrated radiation. This results in more turbulent
786 heat loss at the lake surface and larger variation in the epilimnion temperature
787 (Heiskanen et al., 2015; Zolfaghari et al., 2017). The results from Guseva et al. (2020)
788 suggested that different 1D lake models respond similarly to changes in water clarity
789 and that the thermocline depth increases in clear waters. However, the simulation
790 results showed a slight increase in the thermocline depth when larger light extinction
791 coefficients were used, which is indicated by the reduced negative biases in KD
792 compared with those in CTL (Figure 10a). Although the direct influence of penetrated
793 radiation is restricted in shallow layers, it seems that this heating effect has extended
794 down to approximately 15 m since June (Figure 7a). This could possibly contribute to
795 a deepening of the thermocline. The results also showed that a larger light extinction

796 coefficient generated a thicker metalimnion, which corresponds to the linear
797 relationship deduced from in situ water temperature measurements in Lake Qiandaohu,
798 where a negative correlation between metalimnion thickness and water transparency
799 was found (Zhang et al., 2014). Therefore, it can be tentatively concluded that the
800 response of lake stratification to changes in water clarity may differ in lakes with
801 different depths and thermal regimes. It is difficult to determine the influence of light
802 attenuation on lake stratification because research on this parameter at regional or
803 global scales is still lacking. This literature deficiency may be attributed to insufficient
804 high-frequency measurements of water clarity and water temperature. Satellite-
805 derived series of water transparency combined with lake models may shed more light
806 on this issue.

807 **4.2.2. Initial lake water temperature in monomictic lakes**

808 Sensitivity experiment of the calibrated initial lake temperature profile showed
809 that this modification is crucial for generating realistic hypolimnion temperatures
810 even though the influence of changes in the initial lake temperature profile on LSWT
811 did not last for more than one month. This is unsurprising given that LSWT is driven
812 by the surface energy balance, and its variation can be captured by lake models even
813 in the absence of a reasonable subsurface temperature (Stepanenko et al., 2013).
814 Monomictic lakes do not experience complete overturn in winter and thus cannot reset
815 the deep water temperature like dimictic lakes. Therefore, the underestimation of the
816 hypolimnion temperature in monomictic lakes induced by initial conditions implies

817 insufficient heat storage and could eventually lead to shifts in thermal dynamic
818 processes during long-term simulations (Perroud et al., 2009).

819 **4.2.3. Simulating heat transfer in 1D lake models**

820 The eddy diffusivity parameterization based on Henderson-Sellers (1985)
821 struggles to simulate the mixing strength in deep lakes (Perroud et al., 2009;
822 Stepanenko et al., 2010; Thiery et al., 2014b). Despite that, this type of model has
823 been used widely in lake simulations because of its flexibility, which allows it to
824 produce acceptable results without considerable modification (Martynov et al., 2010).
825 Our results confirmed that the tuned model can simulate seasonal variation of the lake
826 thermal structure with reasonable error during summer, suggesting that this model can
827 be further applied to simulations in which the interannual variations of the lake
828 thermal regime matter. It is believed that the 1D mixing processes can be theoretically
829 tuned to imitate the behavior of that in a real lake based on available empirical
830 formulas. But the limitation of original eddy diffusivity could not be completely
831 solved by enlarging or shrinking it, which is a common approach (Bennington et al.,
832 2014; Wu et al., 2020; Xiao et al., 2016). The results suggest that tuning eddy
833 diffusivity affects only the thermal structure in the epilimnion and upper metalimnion
834 as this coefficient decreases exponentially with depth and levels off below the
835 thermocline with a magnitude far less than the molecular diffusivity. This implies
836 little or no turbulence in the modeled deep layer, which is not the case in reality.

837 The vertical structure of the Henderson-Sellers eddy diffusivity raises two

838 questions. First, the heat diffusion between the thermocline and hypolimnion is
839 lacking in the modeled lake; therefore, the water temperature in the lower
840 metalimnion could not be well reproduced. It is apparent that the k_{obs} concaved at
841 depths with large gradients and decreased mildly with increasing depth; in contrast,
842 the k_{sim} dropped sharply and became less than the molecular diffusivity between 15–
843 40 m. Thus, although Lake Qiandaohu formed two zones with steep temperature
844 gradients, it is believed that this conclusion is tenable in other deep lakes. Moreover,
845 ALBM and MTCR-1, which both uses Henderson-Sellers diffusivity, also failed to
846 reproduce the temporal and depth variability of vertical eddy diffusivity in a
847 temperate dimictic lake (Guseva et al., 2020), although the models generated
848 satisfactory thermal structure. Therefore, it is reasonable to infer that this issue not
849 only existed in WRF-Lake, but also in all advective-diffusive models based on the
850 same parameterization method.

851 The next problem is unresolved heat diffusion in the hypolimnion, for example,
852 internal seiches generated from hypolimnetic currents, that transfer wind energy from
853 the lake surface to turbulence at the bottom (Imberger, 1998). This deficiency exists in
854 selected 1D lake models that do not consider internal waves; even the more
855 sophisticated k- ϵ model can only calculate the turbulence above the thermocline
856 (Perroud et al., 2009), and thus the extra parameterization for turbulences in deep
857 layers is required. It has been found that the vertical diffusivity of heat in stratified
858 layers of many lakes can be described as $k = b(N^2)^m$, where m and b are constants

859 related to lake properties (Jassby and Powell, 1975). Therefore, some models such as
860 the PROBE model (Svensson, 1978), the lake component in CLM 4.5, and an offline
861 version of the WRF-Lake model (Wang et al., 2019) adopted this expression to mimic
862 the unresolved mixing process in factual lakes. It is noteworthy that the weight of this
863 additional term must be cautiously selected for a specific lake. Throughout the testing
864 process, this added term was required for certain depths to better simulate the
865 deepening of the metalimnion in the spring and early summer. However, during the
866 decay of summer stratification, this term must be turned off or decreased to prevent
867 over-mixing in the water column. Zhang et al. (2019) also found that the lake module
868 in CLM 4.5 failed to reproduce the transition between stratification and overturn
869 because of this arbitrary attached term, although it still worked well for some lakes
870 (Wang et al., 2019). Overall, it seems that the inclusion of an enhanced term, such as
871 that of other water mixing schemes and parameterization methods for major types of
872 unresolved heat diffusion, is a compromise between computational cost and more
873 complicated three-dimensional hydrodynamic models.

874

875 **5. Conclusions**

876 In the current study, the WRF-Lake model was improved to simulate the lake
877 thermal regime over a monomictic deep Lake Qiandaohu by tuning four key model
878 parameters, i.e., the initial lake water temperature profiles, light extinction coefficients,
879 eddy diffusion coefficients, and the surface roughness lengths. We found that:

880 (1) The modified 1D lake model, WRF-Lake, simulated thermal structure of
881 Lake Qiandaohu with satisfactory performance. The MBE and RMSE of
882 LSWT between simulation results and in situ observations were reduced
883 from $-1.3\text{ }^{\circ}\text{C}$ to $-0.1\text{ }^{\circ}\text{C}$ and $2.9\text{ }^{\circ}\text{C}$ to $1.6\text{ }^{\circ}\text{C}$, respectively. The evolution of
884 lake stratification was well captured, which is indicated by three metrics. For
885 example, the MBE of the thermocline depth decreased from 13.0 m to -1.7 m .

886 (2) The WRF model overpredicted the near-surface wind speed and downward
887 shortwave radiation on the ground by an MBE of 2.7 m s^{-1} and 82.0 W m^{-2} ,
888 respectively. The impacts of high wind speed on simulating LSWT are in
889 contrast to those of enhanced shortwave radiation but cannot be completely
890 offset. The tuned maximum value of eddy diffusivity limited the effects of
891 wind speed on mixing strength in the subsurface water layers.

892 (3) The initial lake water temperature determined the magnitude of the water
893 temperature in the hypolimnion, which seldom experiences the water–air heat
894 exchange caused by in complete mixing events in deep lakes. The light
895 extinction coefficients and surface roughness lengths have the greatest
896 impact on LSWT by governing the penetration of shortwave radiation in
897 water layers and the exchange efficiency of heat and water vapor at the lake
898 surface. However, they still slightly improve the model performance in
899 simulating subsurface water temperature. Modifications of the eddy
900 diffusivity improved the model performance in simulating the strength of

901 stratification.

902 (4) The Schmidt stability of Lake Qiandaohu varied with LSWT and was well
903 simulated by the modified WRF-Lake model. Development of the
904 thermocline from June to October is difficult to reproduce. The modified
905 WRF-Lake reduced the annual MBE of the thermocline depth from -5.8 m to
906 1.0 m. The temporal variation of lake number and Wedderburn number
907 derived from the simulation results agreed with those of the observations,
908 although the magnitude showed negative biases. The large values of Schmidt
909 stability and low values of lake number and Wedderburn number demonstrate
910 that Lake Qiandaohu was strongly thermally stratified throughout the year,
911 and the wind-driven internal waves in deep water and mixing were weak.

912 Thus, our results demonstrated that the modified WRF-Lake model could
913 simulate LSWT and evolution of lake stratification with the lowest MBE and RMSE,
914 which contributes to improvements in simulating lake thermal dynamics. Although
915 geomorphology and optical characteristics differ between lakes, the revised version of
916 WRF-Lake can be generalized to other study sites after minor modifications. Finally,
917 more lake water temperature measurements are required to improve the
918 representativeness of the mixing process parameterization scheme and enhance
919 overall model performance.

920

921 **Acknowledgments**

922 This work was supported by the National Natural Science Foundation of China (Grant
923 Nos. 41922005 and 41930760) and NIGLAS foundation (E1SL002). The computing
924 resources granted by the Supercomputing Center of Lanzhou University are
925 appreciated.

926

927 **References**

- 928 Anderson, E.J. et al., 2021. Seasonal overturn and stratification changes drive deep-
929 water warming in one of Earth's largest lakes. *Nature Communications*, 12(1):
930 1688. DOI:10.1038/s41467-021-21971-1
- 931 Avolio, E. et al., 2017. Sensitivity analysis of WRF model PBL schemes in simulating
932 boundary-layer variables in southern Italy: An experimental campaign.
933 *Atmospheric Research*, 192: 58-71. DOI:10.1016/j.atmosres.2017.04.003
- 934 Balsamo, G. et al., 2012. On the contribution of lakes in predicting near-surface
935 temperature in a global weather forecasting model. *Tellus A: Dynamic*
936 *Meteorology and Oceanography*, 64(1). DOI:10.3402/tellusa.v64i0.15829
- 937 Bennington, V., Notaro, M., Holman, K.D., 2014. Improving climate sensitivity of
938 deep lakes within a regional climate model and its impact on simulated climate.
939 *Journal of Climate*, 27(8): 2886-2911. DOI:10.1175/JCLI-D-13-00110.1
- 940 Bruce, L.C. et al., 2018. A multi-lake comparative analysis of the General Lake Model
941 (GLM): Stress-testing across a global observatory network. *Environmental*
942 *Modelling & Software*, 102: 274-291. DOI:10.1016/j.envsoft.2017.11.016
- 943 Chen, F., Dudhia, J., 2001. Coupling an advanced land surface-hydrology model with
944 the Penn State-NCAR MM5 modeling system. Part I: Model implementation
945 and sensitivity. *Monthly Weather Review*, 129(4): 569-585.
946 DOI:10.1175/1520-0493(2001)129<0569:Caalsh>2.0.Co;2
- 947 Chen, F. et al., 2011. The integrated WRF/urban modelling system: development,
948 evaluation, and applications to urban environmental problems. *International*
949 *Journal of Climatology*, 31(2): 273-288. DOI:10.1002/joc.2158
- 950 Dai, Y. et al., 2018a. The lake scheme of the Common Land Model and its
951 performance evaluation. *Chinese Science Bulletin*, 63(28-29): 3002-3021.
952 DOI:10.1360/n972018-00609
- 953 Dai, Y., Yao, T., Li, X., Ping, F., 2018b. The impact of lake effects on the temporal and
954 spatial distribution of precipitation in the Nam Co basin, Tibetan Plateau.
955 *Quaternary International*, 475: 63-69. DOI:10.1016/j.quaint.2016.01.075
- 956 Donis, D. et al., 2021. Stratification strength and light climate explain variation in
957 chlorophyll *a* at the continental scale in a European multilake survey in a

958 heatwave summer. *Limnology and Oceanography*, 66(12): 4314-4333.
959 DOI:10.1002/lno.11963

960 Edinger, J., Duttweiler, D., Geyer, J., 1968. The response of water temperature to
961 meteorological conditions. *Water Resources Research*, 4.
962 DOI:10.1029/WR004i005p01137

963 Gu, H., Jin, J., Wu, Y., Ek, M.B., Subin, Z.M., 2015. Calibration and validation of
964 lake surface temperature simulations with the coupled WRF-lake model.
965 *Climatic Change*, 129(3): 471-483. DOI:10.1007/s10584-013-0978-y

966 Gu, H., Ma, Z., Li, M., 2016. Effect of a large and very shallow lake on local summer
967 precipitation over the Lake Taihu basin in China. *Journal of Geophysical*
968 *Research: Atmospheres*, 121(15): 8832-8848. DOI:10.1002/2015jd024098

969 Guo, M. et al., 2021. Validation and sensitivity analysis of a 1 - D lake model across
970 global lakes. *Journal of Geophysical Research: Atmospheres*, 126(4).
971 DOI:10.1029/2020jd033417

972 Guseva, S. et al., 2020. Multimodel simulation of vertical gas transfer in a temperate
973 lake. *Hydrology and Earth System Sciences*, 24(2): 697-715.
974 DOI:10.5194/hess-24-697-2020

975 He, J. et al., 2020. The first high-resolution meteorological forcing dataset for land
976 process studies over China. *Scientific Data*, 7(1): 1-11.

977 Heiskanen, J.J. et al., 2015. Effects of water clarity on lake stratification and lake -
978 atmosphere heat exchange. *Journal of Geophysical Research: Atmospheres*,
979 120(15): 7412-7428. DOI:10.1002/2014jd022938

980 Henderson-Sellers, B., 1985. New formulation of eddy diffusion thermocline models.
981 *Applied Mathematical Modelling*, 9(6): 441-446. DOI:10.1016/0307-
982 904X(85)90110-6

983 Hersbach, H. et al., 2020. The ERA5 global reanalysis. *Quarterly Journal of the Royal*
984 *Meteorological Society*, 146(730): 1999-2049. DOI:10.1002/qj.3803

985 Hong, S.-Y., Noh, Y., Dudhia, J., 2006. A new vertical diffusion package with an
986 explicit treatment of entrainment processes. *Monthly Weather Review*, 134(9):
987 2318-2341. DOI:10.1175/mwr3199.1

988 Hostetler, S.W., Bartlein, P.J., 1990. Simulation of lake evaporation with application
989 to modeling lake level variations of Harney - Malheur Lake, Oregon. *Water*
990 *Resources Research*, 26(10): 2603-2612.

991 Huang, A. et al., 2019. Evaluating and improving the performance of three 1-D lake
992 models in a large deep lake of the central Tibetan Plateau. *Journal of*
993 *Geophysical Research: Atmospheres*, 124(6): 3143-3167.
994 DOI:10.1029/2018JD029610

995 Imberger, J., 1998. Flux paths in a stratified lake: A review. *Physical processes in*
996 *lakes and oceans*, 54: 1-17.

997 Imberger, J., Patterson, J.C., 1989. Physical limnology. *Advances in applied*
998 *mechanics*, 27: 303-475.

999 Janjic, Z.I., 1994. The step-mountain eta coordinate model: further developments of

1000 the convection, viscous sublayer, and turbulence closure schemes. *Monthly*
1001 *Weather Review*, 122(5): 927-945. DOI:10.1175/1520-
1002 0493(1994)122<0927:TSMECM>2.0.CO;2

1003 Jassby, A., Powell, T., 1975. Vertical patterns of eddy diffusion during stratification in
1004 Castle Lake, California 1. *Limnology and oceanography*, 20(4): 530-543.

1005 Jiménez, P.A., Dudhia, J., 2012. Improving the representation of resolved and
1006 unresolved topographic effects on surface wind in the WRF model. *Journal of*
1007 *Applied Meteorology and Climatology*, 51(2): 300-316. DOI:10.1175/jamc-d-
1008 11-084.1

1009 Jiménez, P.A. et al., 2012. A revised scheme for the WRF surface layer formulation.
1010 *Monthly Weather Review*, 140(3): 898-918. DOI:10.1175/mwr-d-11-00056.1

1011 Jousse, A., Hall, A., Sun, F., Teixeira, J., 2016. Causes of WRF surface energy fluxes
1012 biases in a stratocumulus region. *Climate Dynamics*, 46(1): 571-584.

1013 Kraemer, B.M. et al., 2015. Morphometry and average temperature affect lake
1014 stratification responses to climate change. *Geophysical Research Letters*,
1015 42(12): 4981-4988. DOI:10.1002/2015GL064097

1016 Kumar, P., Bhattacharya, B.K., Pal, P., 2015. Evaluation of weather research and
1017 forecasting model predictions using micrometeorological tower observations.
1018 *Boundary-Layer Meteorology*, 157(2): 293-308.

1019 Li, Y.-H., 1973. Vertical eddy diffusion coefficient in Lake Zürich. *Schweizerische*
1020 *Zeitschrift für Hydrologie*, 35(1): 1-7.

1021 Lim, J.-O.J., Hong, S.Y., 2006. The WRF Single-Moment 6-Class Microphysics
1022 Scheme (WSM6). *Asia-Pacific Journal of Atmospheric Sciences*, 42(2): 129-
1023 151.

1024 Liu, M. et al., 2019. Thermal stratification dynamics in a large and deep subtropical
1025 reservoir revealed by high-frequency buoy data. *Sci. Total Environ.*, 651(Pt 1):
1026 614-624. DOI:10.1016/j.scitotenv.2018.09.215

1027 MacIntyre, S., Flynn, K.M., Jellison, R., Romero, J.R., 1999. Boundary mixing and
1028 nutrient fluxes in Mono Lake, California. *Limnology and Oceanography*, 44(3):
1029 512-529.

1030 Martynov, A., Sushama, L., Laprise, R., 2010. Simulation of temperate freezing lakes
1031 by one-dimensional lake models: performance assessment for interactive
1032 coupling with regional climate models. *Boreal Environment Research*, 15:
1033 143-164.

1034 Mironov, D.V., 2008. Parameterization of lakes in numerical weather prediction:
1035 Description of a lake model, DWD.

1036 Oleson, K. et al., 2004. Technical description of the Community Land Model (CLM).
1037 Oleson, K.W. et al., 2013. Technical description of version 4.5 of the Community
1038 Land Model (CLM) (No. NCAR/TN-503+STR).
1039 DOI:doi:10.5065/D6RR1W7M

1040 Pan, X., Li, X., 2011. Validation of WRF model on simulating forcing data for Heihe
1041 River Basin. *Sciences in Cold and Arid Regions*, 3(4): 344-357.

-
- 1042 Perroud, M., Goyette, S., Martynov, A., Beniston, M., Annevillec, O., 2009.
1043 Simulation of multiannual thermal profiles in deep Lake Geneva: A
1044 comparison of one-dimensional lake models. *Limnology and Oceanography*,
1045 54(5): 1574-1594. DOI:10.4319/lo.2009.54.5.1574
- 1046 Piccolroaz, S., Woolway, R.I., Merchant, C.J., 2020. Global reconstruction of
1047 twentieth century lake surface water temperature reveals different warming
1048 trends depending on the climatic zone (vol 35, pg 817, 2020). *Climatic*
1049 *Change*, 160(3): 443-443. DOI:10.1007/s10584-020-02720-7
- 1050 Powell, T., Jassby, A., 1974. The estimation of vertical eddy diffusivities below the
1051 thermocline in lakes. *Water Resources Research*, 10(2): 191-198.
- 1052 Qi, W., Liu, J., Yang, H., Chen, D., Feng, L., 2022. Assessments and Corrections of
1053 GLDAS2.0 Forcing Data in Four Large Transboundary Rivers in the Tibetan
1054 Plateau and Northeast China. *Earth and Space Science*, 9(1): e2020EA001576.
1055 DOI:10.1029/2020EA001576
- 1056 Read, J.S. et al., 2011. Derivation of lake mixing and stratification indices from high-
1057 resolution lake buoy data. *Environmental Modelling & Software*, 26(11):
1058 1325-1336. DOI:10.1016/j.envsoft.2011.05.006
- 1059 Read, J.S., Rose, K.C., 2013. Physical responses of small temperate lakes to variation
1060 in dissolved organic carbon concentrations. *Limnology and Oceanography*,
1061 58(3): 921-931.
- 1062 Richardson, D.C. et al., 2017. Transparency, geomorphology and mixing regime
1063 explain variability in trends in lake temperature and stratification across
1064 Northeastern North America (1975–2014). *Water*, 9(6): 442.
- 1065 Rose, K.C., Winslow, L.A., Read, J.S., Hansen, G.J.A., 2016. Climate-induced
1066 warming of lakes can be either amplified or suppressed by trends in water
1067 clarity. *Limnology and Oceanography Letters*, 1(1): 44-53.
1068 DOI:10.1002/lo12.10027
- 1069 Ruiz-Arias, J.A., Arbizu-Barrena, C., Santos-Alamillos, F.J., Tovar-Pescador, J., Pozo-
1070 Vázquez, D., 2016. Assessing the surface solar radiation budget in the WRF
1071 Model: A spatiotemporal analysis of the bias and its causes. *Monthly Weather*
1072 *Review*, 144(2): 703-711. DOI:10.1175/mwr-d-15-0262.1
- 1073 Schmid, M., Hunziker, S., Wüest, A., 2014. Lake surface temperatures in a changing
1074 climate: a global sensitivity analysis. *Climatic Change*, 124(1-2): 301-315.
1075 DOI:10.1007/s10584-014-1087-2
- 1076 Schmid, M., Read, J., 2021. Heat Budget of Lakes, Reference Module in Earth
1077 Systems and Environmental Sciences. Elsevier. DOI:10.1016/B978-0-12-
1078 819166-8.00011-6
- 1079 Schmidt, W., 1928. Über Die Temperatur-Und Stabili-Tätsverhältnisse Von Seen.
1080 *Geografiska Annaler*, 10(1-2): 145-177.
- 1081 Shatwell, T., Adrian, R., Kirillin, G., 2016. Planktonic events may cause polymictic-
1082 dimictic regime shifts in temperate lakes. *Sci Rep*, 6: 24361.
1083 DOI:10.1038/srep24361

1084 Shi, Y. et al. (2022). Drivers of warming in Lake Nam Co on Tibetan Plateau over the
1085 past 40 years. *Journal of Geophysical Research: Atmospheres*, 127,
1086 e2021JD036320. DOI: 10.1029/2021JD036320

1087 Skamarock, W.C. et al., 2019. A description of the advanced research WRF model
1088 version 4. National Center for Atmospheric Research: Boulder, CO, USA: 145.

1089 Stauffer, D.R., Seaman, N.L., 1994. Multiscale four-dimensional data assimilation.
1090 *Journal of Applied Meteorology*, 33(3): 416-434. DOI:10.1175/1520-
1091 0450(1994)033<0416:Mfdda>2.0.Co;2

1092 Stepanenko, V. et al., 2010. First steps of a lake model intercomparison project:
1093 LakeMIP. *Boreal Environment Research*, 15: 191-202.

1094 Stepanenko, V. et al., 2014. Simulation of surface energy fluxes and stratification of a
1095 small boreal lake by a set of one-dimensional models. *Tellus A: Dynamic
1096 Meteorology and Oceanography*, 66(1): 21389.
1097 DOI:10.3402/tellusa.v66.21389

1098 Stepanenko, V.M. et al., 2013. A one-dimensional model intercomparison study of
1099 thermal regime of a shallow, turbid midlatitude lake. *Geoscientific Model
1100 Development*, 6(4): 1337-1352. DOI:10.5194/gmd-6-1337-2013

1101 Su, R. et al., 2022. Summer lake destratification phenomenon: A peculiar deep lake on
1102 the Tibetan Plateau. *Frontiers in Earth Science*, 10: 839151.
1103 DOI:10.3389/feart.2022.839151

1104 Subin, Z.M., Riley, W.J., Mironov, D., 2012. An improved lake model for climate
1105 simulations: Model structure, evaluation, and sensitivity analyses in CESM1.
1106 *Journal of Advances in Modeling Earth Systems*, 4.
1107 DOI:10.1029/2011ms000072

1108 Svensson, U., 1978. A mathematical model of the seasonal thermocline. Institutionen
1109 För Teknisk Vattenresurslära, Lunds Tekniska Högskola, Lunds

1110 Thiery, W. et al., 2014a. Understanding the performance of the FLake model over two
1111 African Great Lakes. *Geoscientific Model Development*, 7(1): 317-337.
1112 DOI:10.5194/gmd-7-317-2014

1113 Thiery, W.I.M. et al., 2014b. LakeMIP Kivu: evaluating the representation of a large,
1114 deep tropical lake by a set of one-dimensional lake models. *Tellus A: Dynamic
1115 Meteorology and Oceanography*, 66(1). DOI:10.3402/tellusa.v66.21390

1116 Thompson, R., 1980. Response of a numerical model of a stratified lake to wind stress,
1117 *Proc. Second Int. Symp. Stratified Flows, IAHR, 1980*, pp. 562-570.

1118 Till, A., Rypel, A.L., Bray, A., Fey, S.B., 2019. Fish die-offs are concurrent with
1119 thermal extremes in north temperate lakes. *Nature Climate Change*, 9(8): 637-
1120 641. DOI:10.1038/s41558-019-0520-y

1121 Wang, F. et al., 2019. Evaluation of the WRF lake module (v1.0) and its
1122 improvements at a deep reservoir. *Geoscientific Model Development*, 12(5):
1123 2119-2138. DOI:10.5194/gmd-12-2119-2019

1124 Wen, L., Lyu, S., li, Z., Zhao, L., Nagabhatla, N., 2014. Impact of two biggest lakes
1125 on local temperature and precipitation in the Yellow River source region of the

1126 Tibetan Plateau. *Advances in Meteorology*.

1127 Wild, M., 2005. Solar radiation budgets in atmospheric model intercomparisons from
 1128 a surface perspective. *Geophysical Research Letters*, 32(7).

1129 Woolway, R.I., Jennings, E., Carrea, L., 2020. Impact of the 2018 European heatwave
 1130 on lake surface water temperature. *Inland Waters*, 10(3): 322-332.
 1131 DOI:10.1080/20442041.2020.1712180

1132 Woolway, R.I. et al., 2019. Northern Hemisphere Atmospheric Stilling Accelerates
 1133 Lake Thermal Responses to a Warming World. *Geophysical Research Letters*,
 1134 46(21): 11983-11992. DOI:10.1029/2019gl082752

1135 Woolway, R.I. et al., 2021. Phenological shifts in lake stratification under climate
 1136 change. *Nature Communications*, 12(1). DOI:10.1038/s41467-021-22657-4

1137 Woolway, R.I. et al., 2018. Geographic and temporal variations in turbulent heat loss
 1138 from lakes: A global analysis across 45 lakes. *Limnology and Oceanography*,
 1139 63(6): 2436-2449. DOI:10.1002/lno.10950

1140 Wu, Y. et al., 2020. Improvements of the coupled WRF-Lake model over Lake Nam
 1141 Co, Central Tibetan Plateau. *Climate Dynamics*, 55(9-10): 2703-2724.
 1142 DOI:10.1007/s00382-020-05402-3

1143 Xiao, C., Lofgren, B.M., Wang, J., Chu, P.Y., 2016. Improving the lake scheme within
 1144 a coupled WRF - lake model in the Laurentian Great Lakes. *Journal of*
 1145 *Advances in Modeling Earth Systems*, 8(4): 1969-1985.
 1146 DOI:10.1002/2016ms000717

1147 Xu, L., Liu, H., Du, Q., Wang, L., 2016. Evaluation of the WRF-lake model over a
 1148 highland freshwater lake in southwest China. *Journal of Geophysical Research:*
 1149 *Atmospheres*, 121(23): 13,989-14,005. DOI:10.1002/2016jd025396

1150 Yang, F. et al., 2017. Evaluation of multiple forcing data sets for precipitation and
 1151 shortwave radiation over major land areas of China. *Hydrology and Earth*
 1152 *System Sciences*, 21(11): 5805-5821. DOI:10.5194/hess-21-5805-2017

1153 Yang, K., He, J., Tang, W., Qin, J., Cheng, C.C., 2010. On downward shortwave and
 1154 longwave radiations over high altitude regions: Observation and modeling in
 1155 the Tibetan Plateau. *Agricultural and Forest Meteorology*, 150(1): 38-46.

1156 Zamani, B., Koch, M., Hodges, B.R., 2021. A potential tipping point in the thermal
 1157 regime of a warm monomictic reservoir under climate change using three-
 1158 dimensional hydrodynamic modeling. *Inland Waters*, 11(3): 315-334.

1159 Zeng, X., Zhao, M., Dickinson, R.E., 1998. Intercomparison of bulk aerodynamic
 1160 algorithms for the computation of sea surface fluxes using TOGA COARE and
 1161 TAO data. *Journal of Climate*, 11(10): 2628-2644.

1162 Zhang, Q. et al., 2019. Improving lake mixing process simulations in the Community
 1163 Land Model by using K profile parameterization. *Hydrology and Earth System*
 1164 *Sciences*, 23(12): 4969-4982. DOI:10.5194/hess-23-4969-2019

1165 Zhang, Y. et al., 2014. Thermal structure and response to long-term climatic changes
 1166 in Lake Qiandaohu, a deep subtropical reservoir in China. *Limnology and*
 1167 *Oceanography*, 59(4): 1193-1202. DOI:10.4319/lo.2014.59.4.1193

1168 Zolfaghari, K., Duguay, C.R., Kheyrollah Pour, H., 2017. Satellite-derived light
1169 extinction coefficient and its impact on thermal structure simulations in a 1-D
1170 lake model. *Hydrology and Earth System Sciences*, 21(1): 377-391.
1171 DOI:10.5194/hess-21-377-2017
1172

1173 **Supplemental materials to "Numerical simulation of thermal**
1174 **stratification in Lake Qiandaohu using an improved WRF-Lake**
1175 **model "**

1176

1177 Xiwen Wang^{a,b}, Weijia Wang^{b,c}, Yuan He^d, Shulei Zhang^e, Wei Huang^a, R. Iestyn Woolway^f, Kun Shi^{b,c*},

1178 Xiaofan Yang^{d*}

1179

1180 ^aKey Laboratory of Western China's Environmental Systems (Ministry of Education), College of Earth
1181 and Environmental Sciences, Lanzhou University, Lanzhou, 730000, China

1182 ^bTaihu Laboratory for Lake Ecosystem Research, State Key Laboratory of Lake Science and
1183 Environment, Nanjing Institute of Geography and Limnology, Chinese Academy of Sciences, Nanjing
1184 210008, China

1185 ^c University of Chinese Academy of Sciences, Beijing 100049, China

1186 ^dState Key Laboratory of Earth Surface Processes and Resource Ecology, Faculty of Geographical
1187 Science, Beijing Normal University, Beijing 100875, China

1188 ^e School of Atmospheric Sciences, Sun Yat-sen University, Guangzhou, China

1189 ^f School of Ocean Sciences, Bangor University, Menai Bridge, Anglesey, Wales

1190

1191 Corresponding author:

1192 [Kun Shi: kshi@niglas.ac.cn](mailto:kshi@niglas.ac.cn)

1193 [Xiaofan Yang: xfyang@bnu.edu.cn](mailto:xfyang@bnu.edu.cn)

1194

1195 **Contents**

1196 This supplementary material contains Supporting Information 1-2, Figure S1-16, and
1197 Table S1-3.

1198

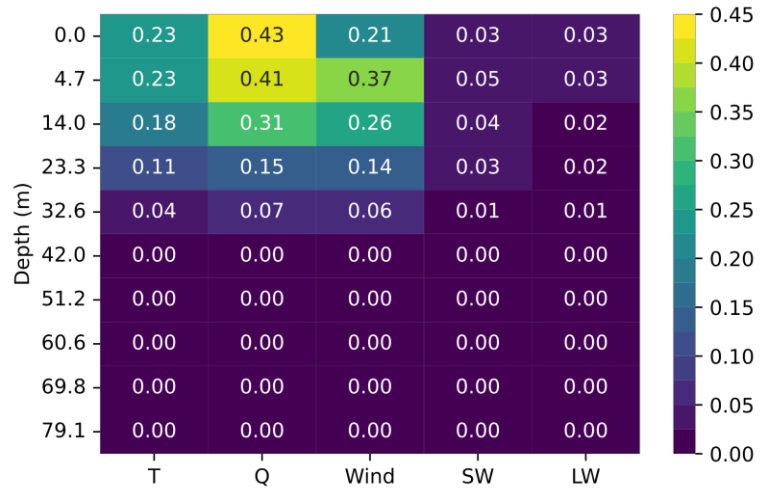
1199 **Supporting information 1: Sensitivity analysis of WRF-Lake in offline mode**

1200 To provide practical guidance for the possible consequences of inaccurate
1201 forcings, we performed a sensitivity analysis by running the default WRF-Lake
1202 offline. In this way the meteorological forcings will not be affected by the lake
1203 condition during simulations. The input forcings come from the ERA5 reanalysis with
1204 hourly temporal and 0.25° spatial resolution. Other settings (e.g., initial conditions)
1205 are the same as CTL. We conducted five sensitivity experiments (Table S1) and a
1206 control experiment (BASE). The mean bias errors against BASE are shown in Figure
1207 S2. It is clear that the influences of overestimated wind speed and shortwave radiation
1208 are mainly on the subsurface water layer at annual scale. High wind speed caused
1209 little cooling effect during summer and increased water temperature in shallow layers
1210 during the cool-down period in the autumn. Our results suggested lake surface water
1211 temperature (averaged over 0-2 m) could increase 0.22 °C if wind speed increases by
1212 1.41 m s⁻¹, and increase 0.03 °C if shortwave radiation increases by 1 W m⁻². The
1213 latter is similar to the findings in Schmid et al. (2014). For the lake thermal structure,
1214 the overestimated shortwave radiation could result in warmer temperature above 20 m.
1215 Stronger wind largely increases the water temperature above 30 m in the autumn.

1216

1217 Table S1 Five experiments for sensitivity analysis.

Case	Description
BASE	Control experiment
T	Increase 2-m air temperature by 1 °C
Q	Increase 2-m specific humidity by 0.001 kg kg ⁻¹
Wind	Increase both 10-m U and V components of wind by 1 m s ⁻¹
SW	Increase downward shortwave radiation at the ground by 1 W m ⁻²
LW	Increase downward longwave radiation at the ground by 1 W m ⁻²



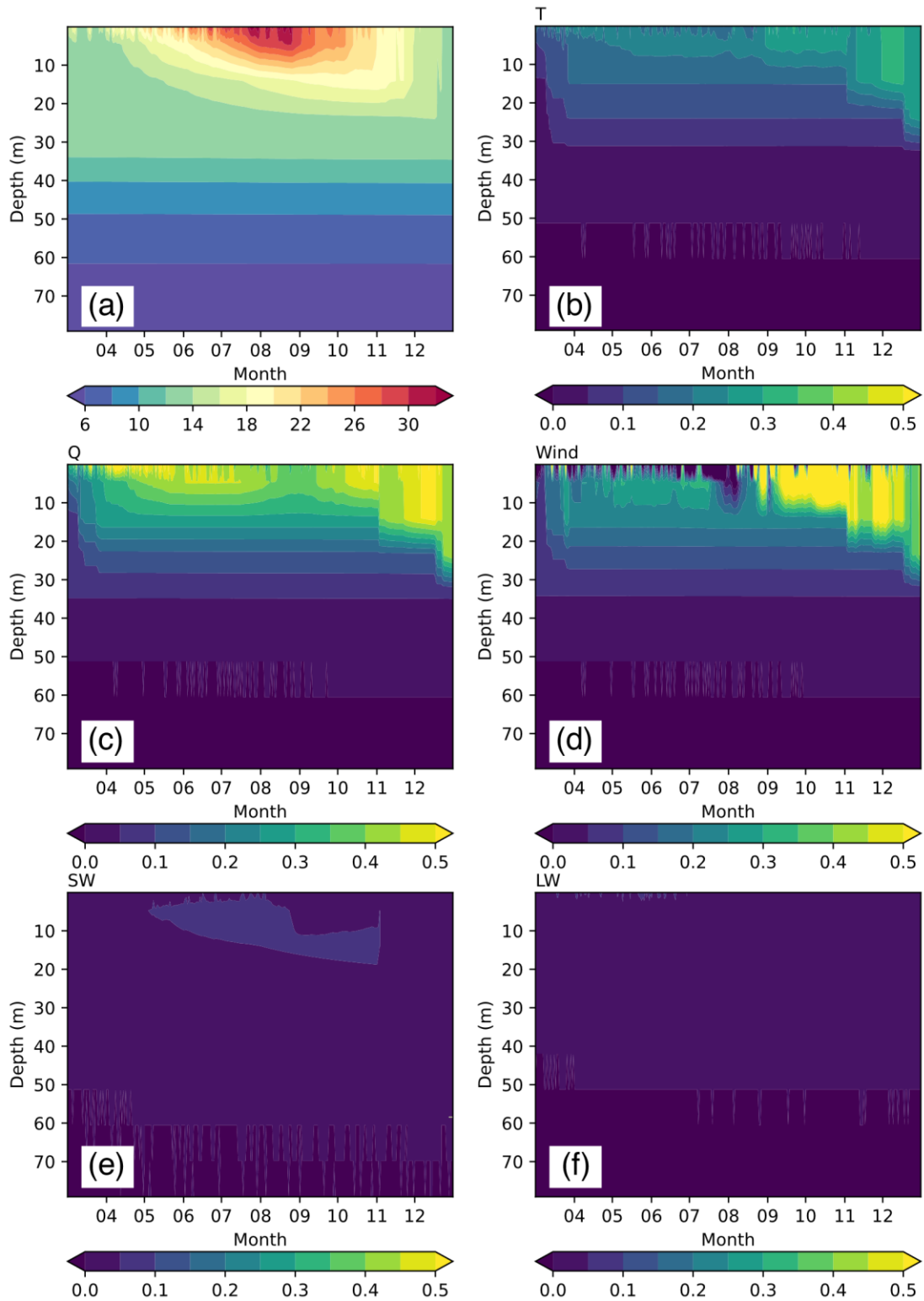
1218

1219

Figure S1 Mean bias error of lake water temperature between BASE and other

1220

experiments during 2016.



1221

1222

1223

1224

Figure S2 (a) Lake water temperature ($^{\circ}\text{C}$) in the BASE experiment and the differences between BASE and (b) T, (c) Q, (d) Wind, (e) SW and (f) LW.

1225 **Supporting information 2: Using a 25-layer discretization method**

1226 We performed two additional numerical experiments using a 25-layer
1227 discretization method (Table S2) based on the CTL and MOD experiment respectively,
1228 denoted as CTL_25 and MOD_25 (Figure S3-4). The results showed that increasing
1229 vertical layers produces smoother water temperature profile during the development
1230 of thermal stratification. The mixing strength above 10 m was promoted, although the
1231 overall distribution of water temperature below 20 m was only slightly affected. The
1232 root mean square error (RMSE) for the surface water temperature (the average of 0-2
1233 m) in MOD_25 is 1.18 °C, smaller than that of MOD (1.59 °C). However, the
1234 negative bias above 20 m and the positive bias below it got worse in MOD_25.

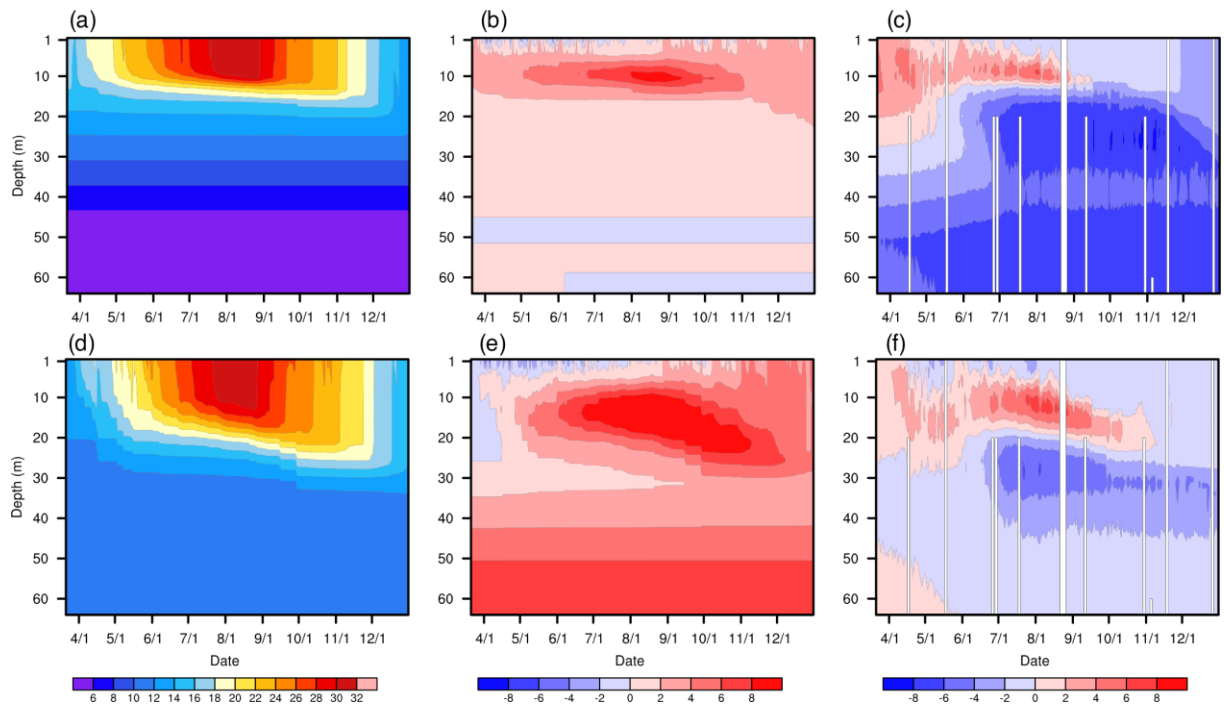
1235

Table S2 The layer thickness and depth of each layer center at Daba buoy (~ 93 m)

1236

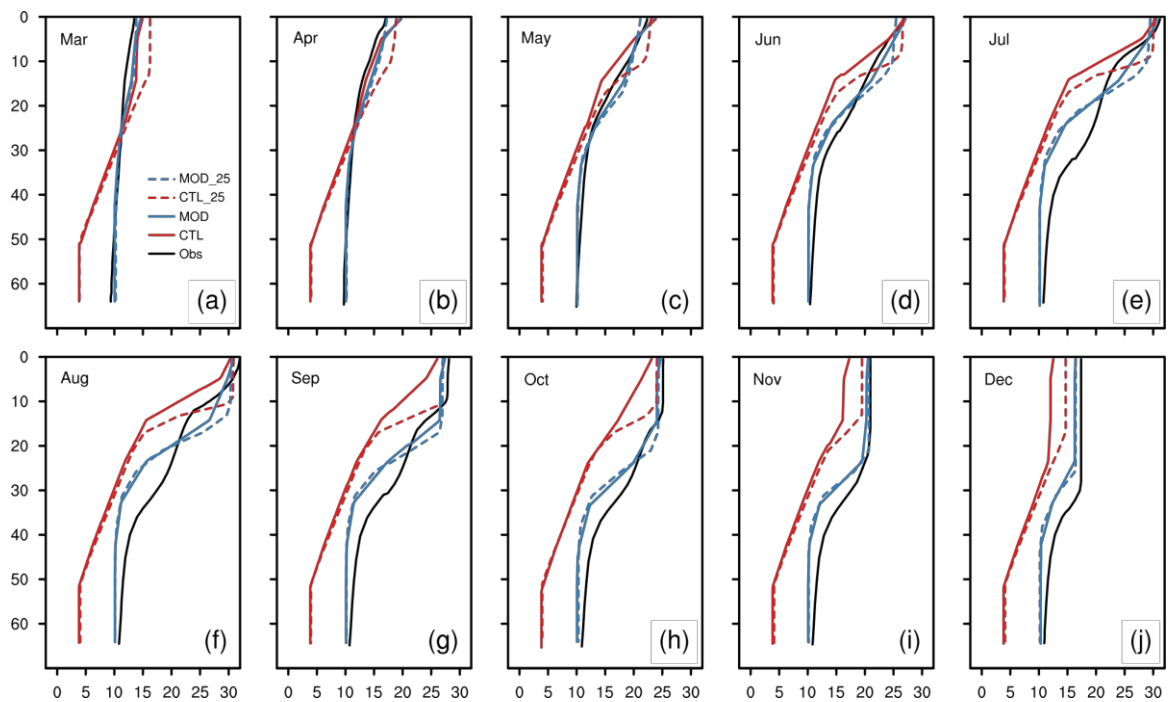
using 25-layer discretization method.

Layer	Thickness (m)	Depth (m)
1	0.1	0.05
2	0.465	0.3325
3	0.465	0.7975
4	0.465	1.2625
5	0.465	1.7275
6	0.93	2.425
7	0.93	3.355
8	0.93	4.285
9	0.93	5.215
10	1.395	6.3775
11	1.395	7.7725
12	1.395	9.1675
13	1.395	10.5625
14	3.72	13.12
15	3.72	16.84
16	4.65	21.025
17	4.65	25.675
18	6.51	31.255
19	6.51	37.765
20	6.51	44.275
21	6.51	50.785
22	9.7185	58.89925
23	9.7185	68.61775
24	9.7185	78.33625
25	9.7185	88.05475



1237
 1238
 1239
 1240
 1241
 1242

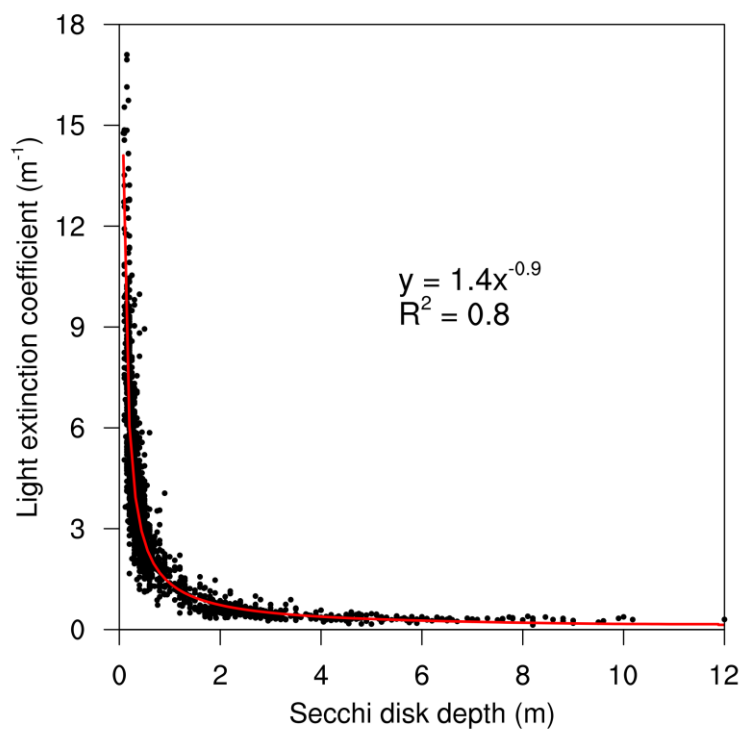
Figure S3 The lake water temperature ($^{\circ}\text{C}$) at Daba simulated by (a) CTL_25 and (d) MOD_25 from 2016-03-21 to 2016-12-31. The differences between CTL and CTL_25 (b), the observations and CTL_25 (c), CTL and MOD_25 (e) and the observations and MOD_25 (f).



1243
 1244
 1245

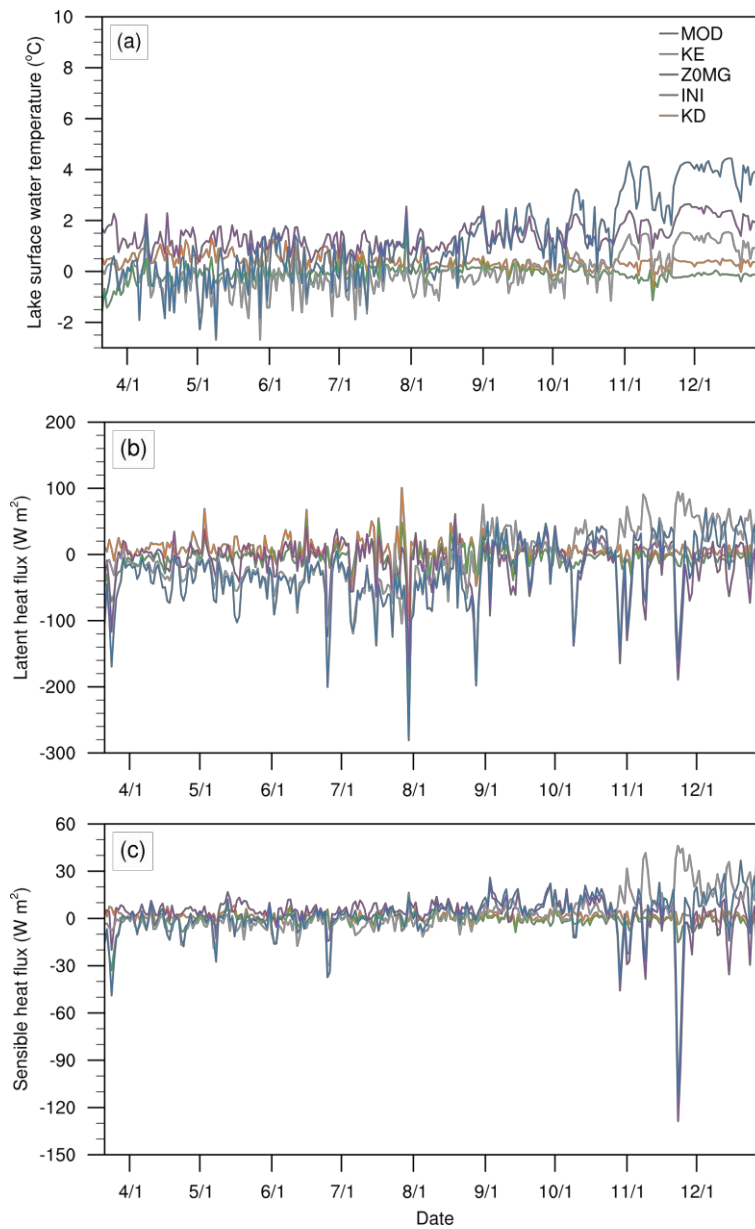
Figure S4 The monthly lake water temperature profile derived from the observations simulated by CTL, MOD, CTL_25 and MOD_25.

1246 Figure S5 Light extinction coefficients in photosynthetically active radiation region
1247 (400–700 nm).



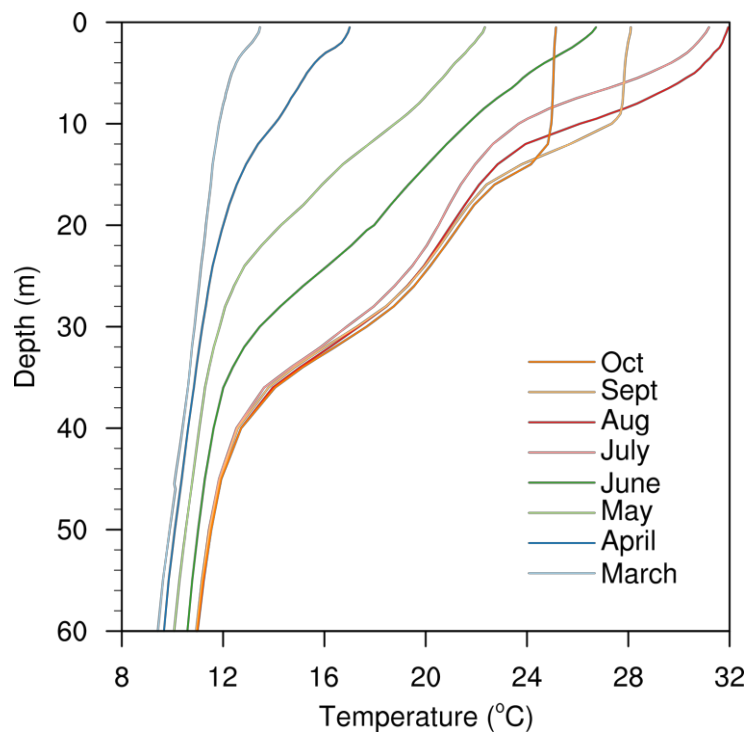
1248

1249 Figure S6 Daily variation of (a) lake surface water temperature ($^{\circ}\text{C}$), (b) sensible heat
1250 flux (W m^{-2}), and (c) latent heat flux (W m^{-2}) differences between CTL and other
1251 sensitivity.



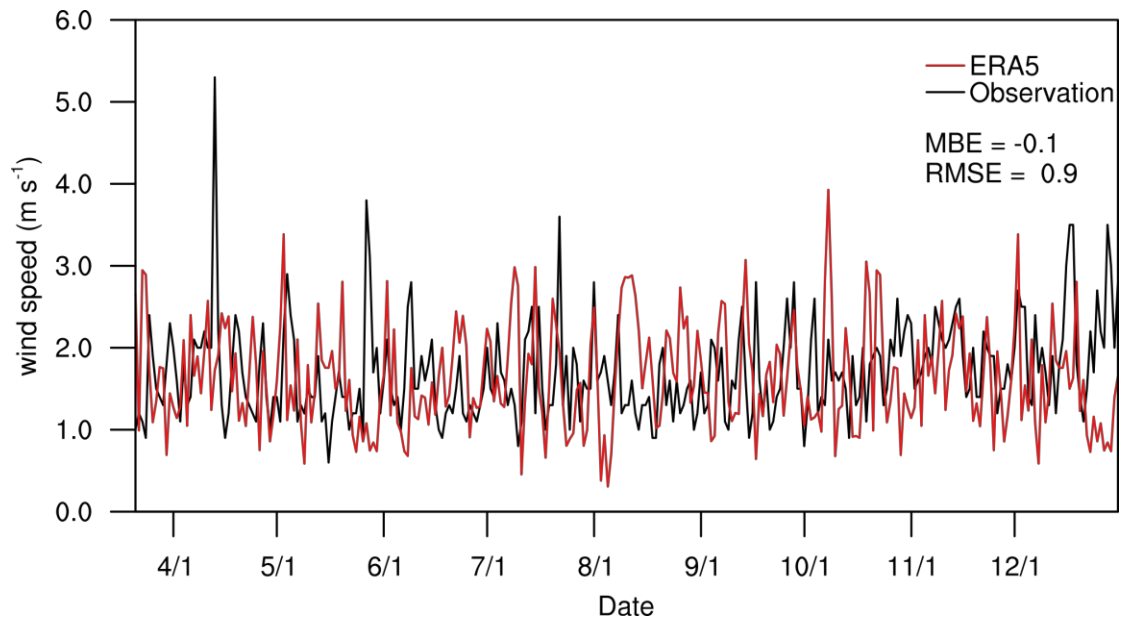
1252

1253 Figure S7 Monthly vertical profiles of the observed water temperature at the Daba
1254 station.



1255

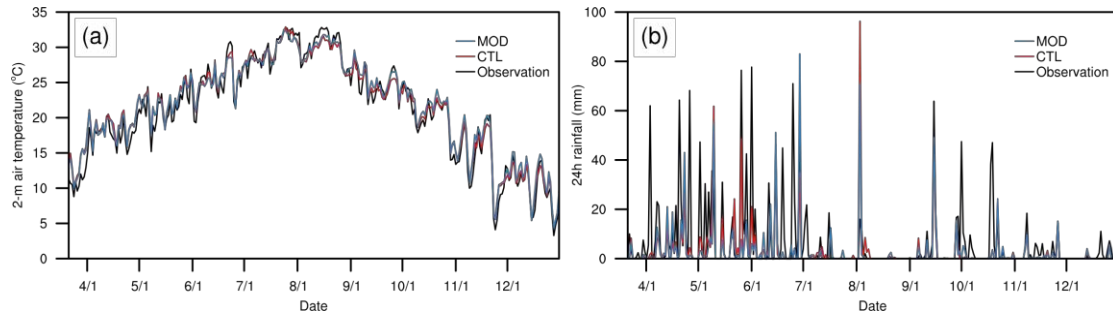
1256 Figure S8 Daily 10-m wind speed (m s^{-1}) from the ERA5 reanalysis (red line) and
1257 observations at the Chun'an weather station (black line). Mean bias error (MBE) and
1258 root mean square error (RMSE) between them are -0.1 m s^{-1} and 0.9 m s^{-1} ,
1259 respectively.



1260

1261

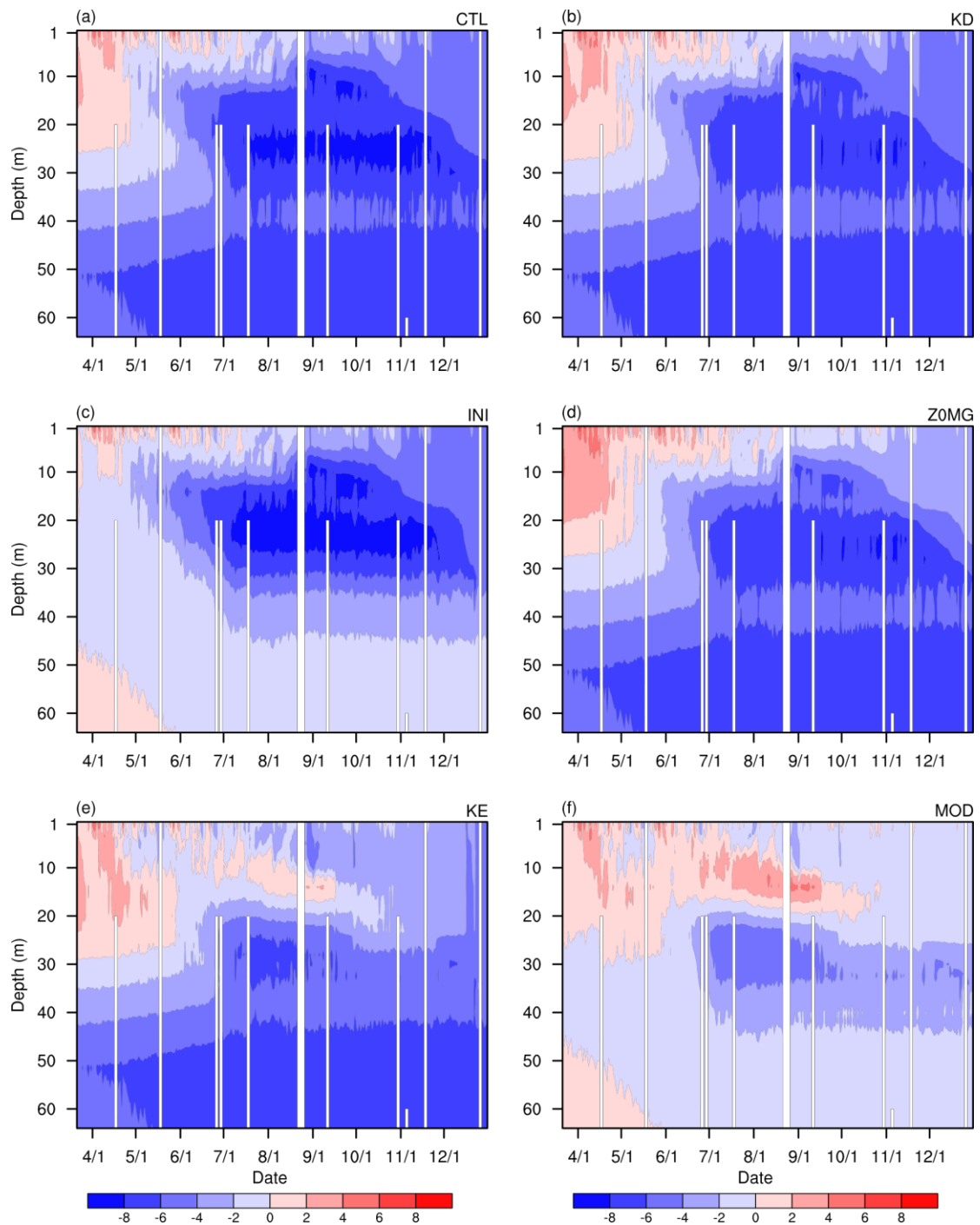
1262 Figure S9 The 2-m air temperature ($^{\circ}\text{C}$) and 24h rainfall (mm) observed by Chun'an
1263 weather station and simulated by CTL and MOD from March 21 2016 and December
1264 31 2016.



1265

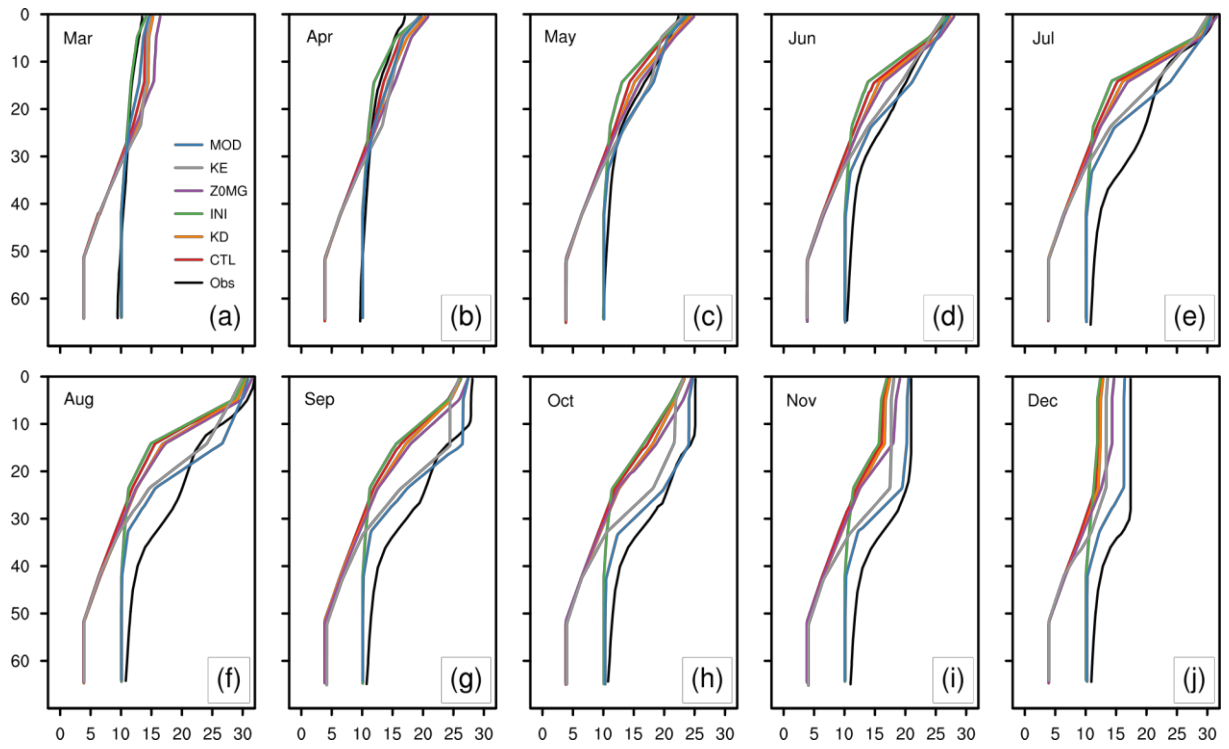
1266

1267 Figure S10 Differences between lake water temperature ($^{\circ}\text{C}$) simulated by (a) CTL, (b)
1268 KD, (c) INI, (d) Z0MG, (e) KE, and (f) MOD.



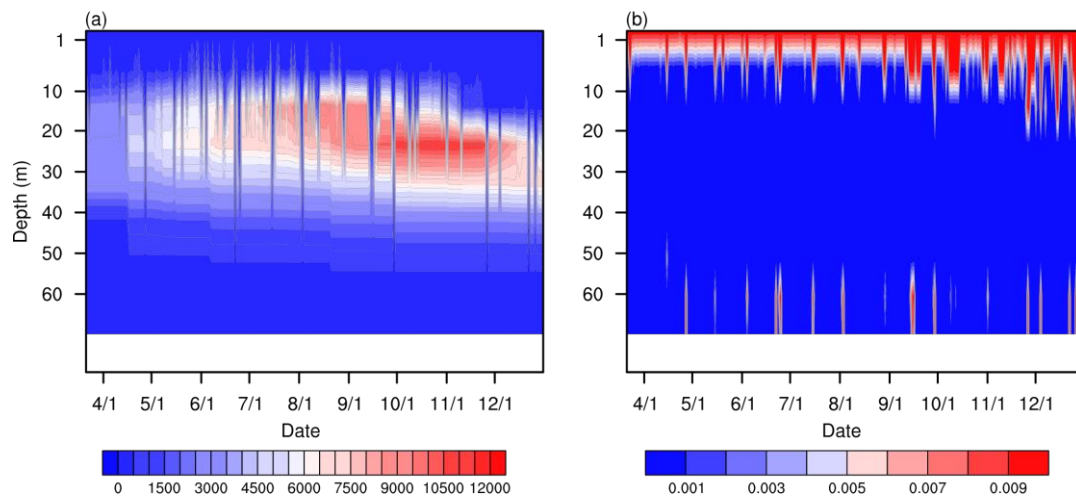
1269

1270 Figure S11 Monthly vertical temperature profiles for the first 65 m water in 2016.



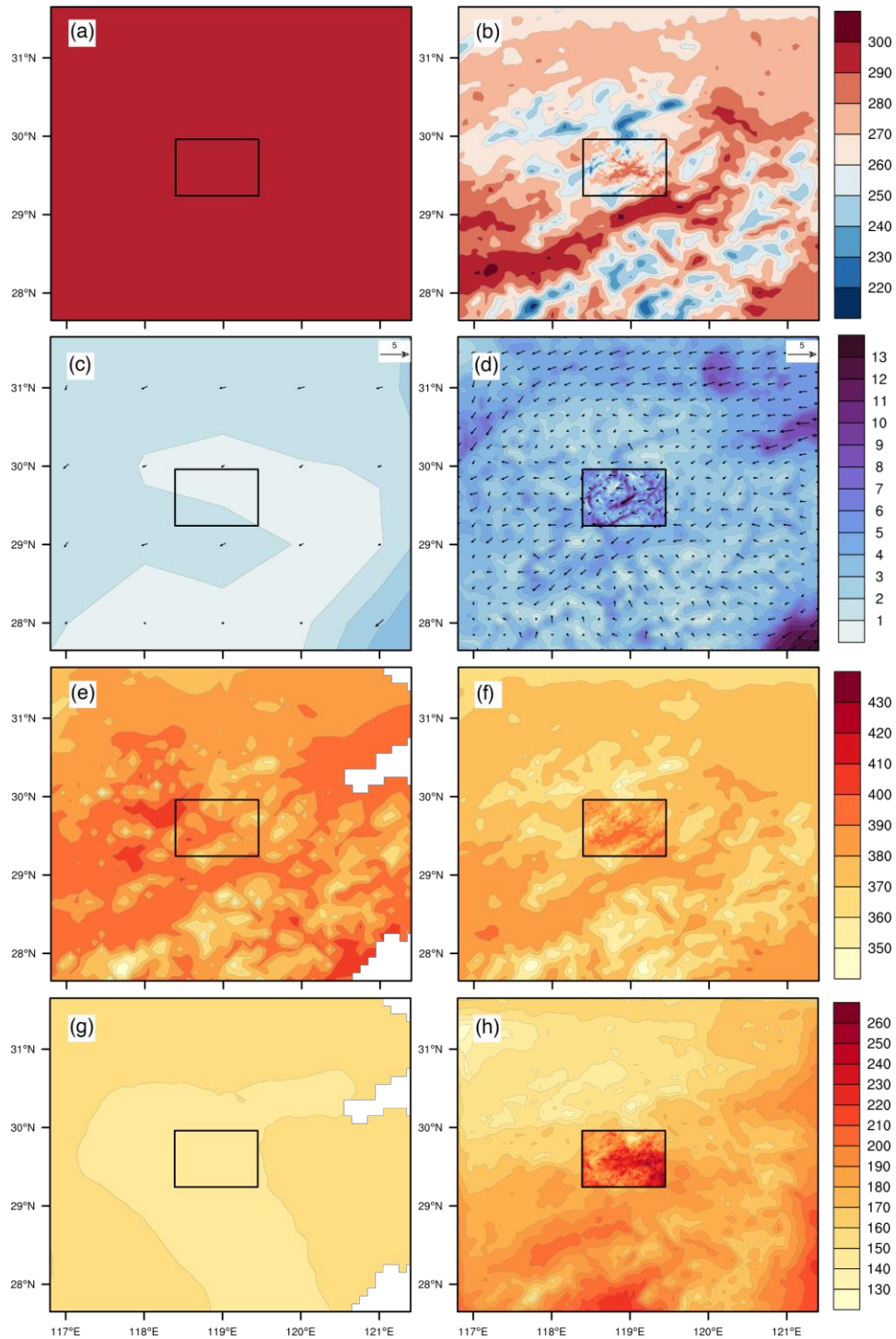
1271

1272 Figure S12 (a) Ri and (b) k_e ($\text{m}^2 \text{s}^{-1}$) at 04:00 UTC each day from 2016-03-21 to
1273 2016-12-31. The blank at the bottom denotes missing values of the last vertical layer.



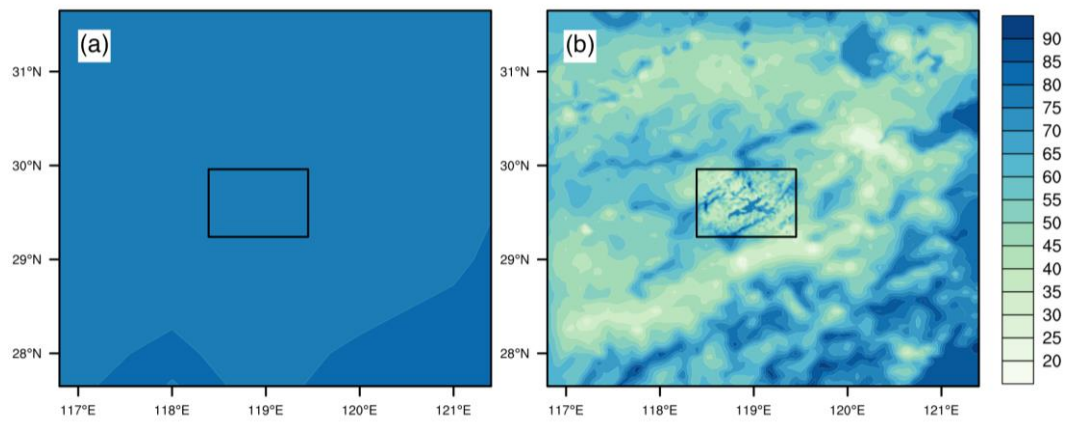
1274

1275 Figure S13 The time-averaged (a-b) 2-m air temperature (K), (c-d) 10-m wind speed
 1276 (m s^{-1}), (e-f) surface downward shortwave radiation (W m^{-2}) and (g-h) surface
 1277 longwave radiation (W m^{-2}) from 2016-03-21 to 2016-12-31. The first column shows
 1278 the reanalysis and the second shows the simulation results. 2-m air temperature and
 1279 10-m wind speed are compared with ERA5. The shortwave and longwave radiation
 1280 are compared with CMFD.



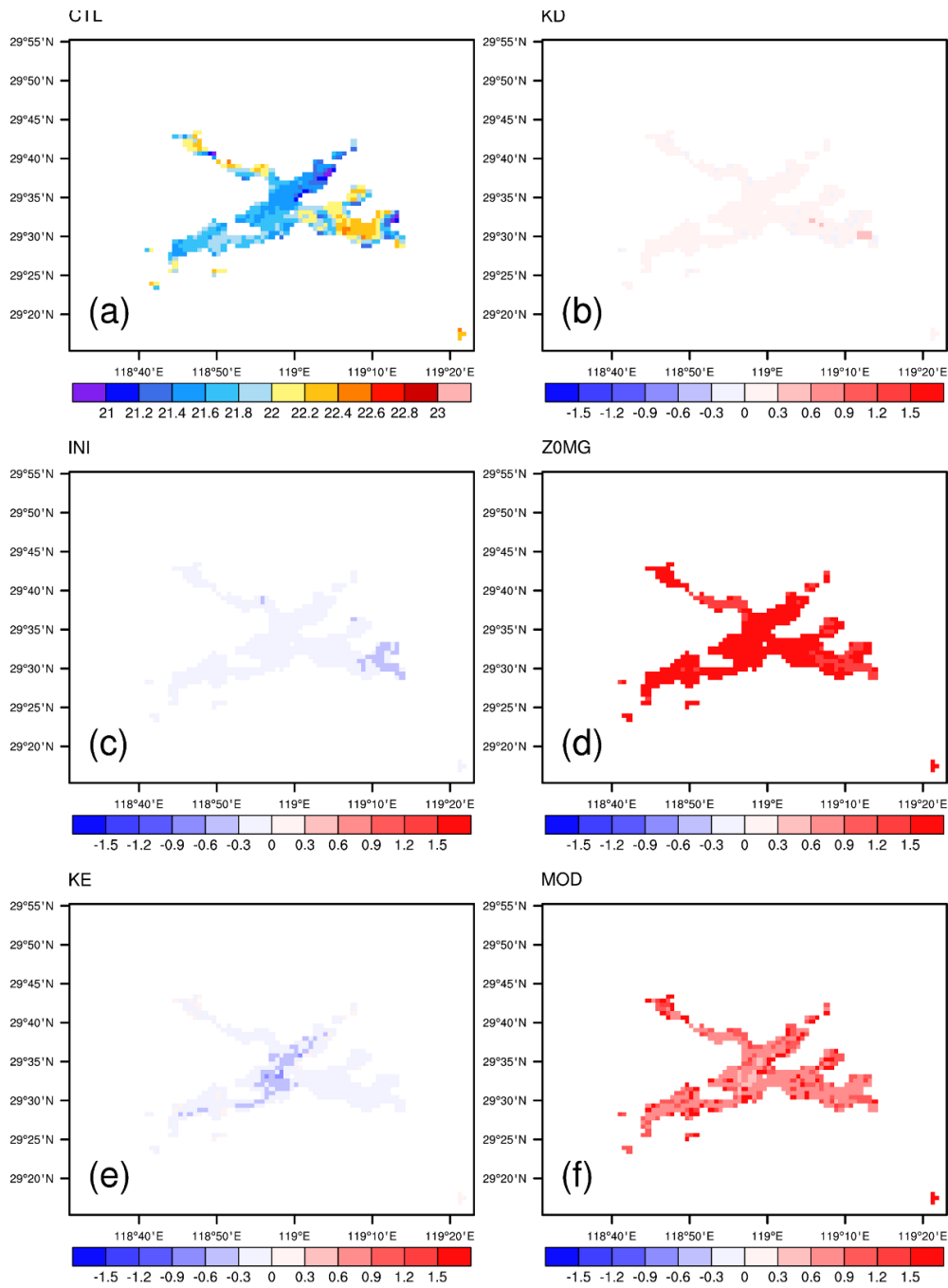
1281

1282 Figure S14 Same as Figure S13 but for the 2-m relative humidity (%), compared with
1283 ERA5.



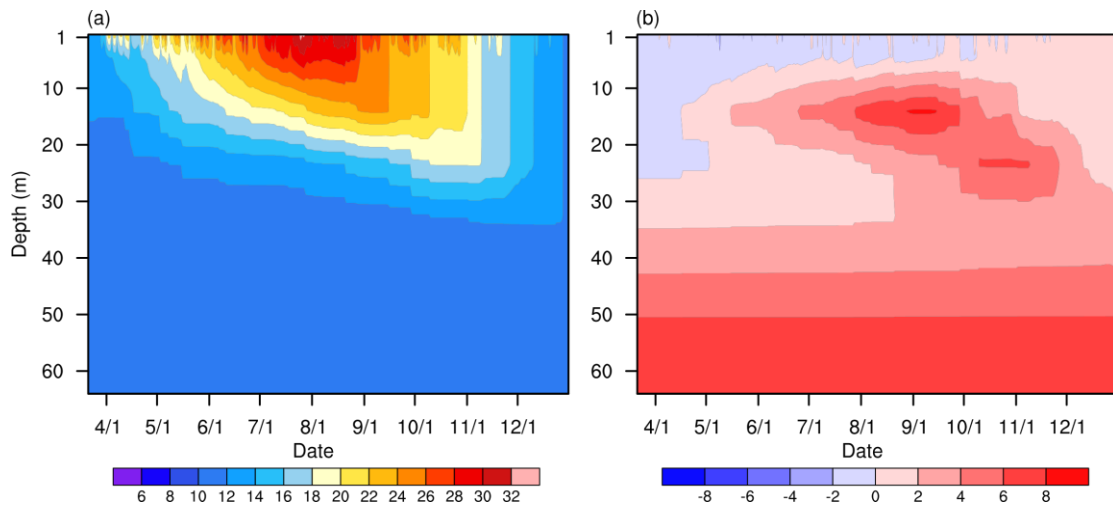
1284

1285 Figure S15 The lake water temperature of the top model layer (0.05 m) of CTL (a)
1286 and its difference against KD (b), INI (c), Z0MG (d), KE (e), and MOD (f).



1287

1288 Figure S16 The simulated lake water temperature ($^{\circ}\text{C}$) and its differences with CTL.



1289

1290 Table S3 Mean bias error (MBE) and root mean square error (RMSE) of lake water
 1291 temperature at different lake depth (0-2 m, 9-11 m, 19-21 m and 39-41 m), bottom
 1292 depth of metalimnion (metaB), thickness of metalimnion (metaTh) and thermocline
 1293 depth (thermD).

	Case	0-2 m	9-11 m	19-21 m	39-41 m	metaB	metaTh	thermD
MBE	CTL	-1.29	-3.59	-5.06	-5.02	12.96	-3.92	-5.8
	KD	-0.89	-2.85	-4.44	-4.83	-13.39	-5.01	-7.85
	INI	-1.38	-4.17	-5.75	-1.87	13.96	-3.28	-5.25
	Z0MG	0.1	-1.9	-4.08	-4.83	12.03	1.34	2.35
	KE	-1.31	-1.17	-1.71	-4.7	15.99	-3.97	-5.5
	KE_INI	-1.5	-1.78	-2.48	-1.65	-4.13	0.13	-0.82
	MOD	-0.08	0.46	-0.6	-1.62	-1.71	0.51	0.95
RMSE	CTL	2.87	4.54	6.04	5.33	18.88	7.51	12.1
	KD	2.76	3.99	5.49	5.14	16.33	8.81	13.12
	INI	2.87	4.85	6.57	2.15	18.51	6.69	11.1
	Z0MG	2.25	3.25	5.21	5.14	18.29	6	9.73
	KE	2.55	2.39	2.7	5	19.62	6.71	10.54
	KE_INI	2.58	2.47	3.01	1.88	9.21	5.01	9.02
	MOD	1.59	1.51	1.25	1.85	8.08	4.74	8.75

1294